

Tracing the kinematics of the whole ram pressure stripped tails in ESO 137-001

Rongxin Luo^{1*}, Ming Sun^{1†}, Pavel Jáchym², Will Waldron¹, Matteo Fossati^{3,4}, Michele Fumagalli^{3,5}, Alessandro Boselli⁶, Françoise Combes⁷, Jeffrey D. P. Kenney⁸, Yuan Li⁹, Max Gronke¹⁰

¹*Department of Physics, University of Alabama in Huntsville, 301 Sparkman Dr NW, Huntsville, AL 35899, USA*

²*Astronomical Institute of the Czech Academy of Sciences, Boční II 1401, 141 00, Prague, Czech Republic*

³*Dipartimento di Fisica G. Occhialini, Università degli Studi di Milano Bicocca, Piazza della Scienza 3, I-20126 Milano, Italy*

⁴*INAF-Osservatorio Astronomico di Brera, via Brera 28, I-20121 Milano, Italy*

⁵*INAF-Osservatorio Astronomico di Trieste, Via G. B. Tiepolo 11, I-34143 Trieste, Italy*

⁶*Aix Marseille Univ, CNRS, CNES, LAM, Marseille, F-13013 France*

⁷*Observatoire de Paris, LERMA, Collège de France, CNRS, PSL Univ, Sorbonne University, UPMC F-75014 Paris, France*

⁸*Yale University Astronomy Department, P.O. Box 208101, New Haven, CT 06520-8101 USA*

⁹*Department of Physics, University of North Texas, Denton, TX 76203, USA*

¹⁰*Max Planck Institut für Astrophysik, Karl-Schwarzschild-Straße 1, D-85748 Garching bei München, Germany*

Accepted XXX. Received YYY; in original form ZZZ

ABSTRACT

Ram pressure stripping (RPS) is an important process to affect the evolution of cluster galaxies and their surrounding environment. We present a large *MUSE* mosaic for ESO 137-001 and its stripped tails, and study the detailed distributions and kinematics of the ionized gas and stars. The warm, ionized gas is detected to at least 87 kpc from the galaxy and splits into three tails. There is a clear velocity gradient roughly perpendicular to the stripping direction, which decreases along the tails and disappears beyond ~ 45 kpc downstream. The velocity dispersion of the ionized gas increases to ~ 80 km s⁻¹ at ~ 20 kpc downstream and stays flat beyond. The stars in the galaxy disc present a regular rotation motion, while the ionized gas is already disturbed by the ram pressure. Based on the observed velocity gradient, we construct the velocity model for the residual galactic rotation in the tails and discuss the origin and implication of its fading with distance. By comparing with theoretical studies, we interpreted the increased velocity dispersion as the result of the oscillations induced by the gas flows in the galaxy wake, which may imply an enhanced degree of turbulence there. We also compare the kinematic properties of the ionized gas and molecular gas from *ALMA*, which shows they are co-moving and kinematically mixed through the tails. Our study demonstrates the great potential of spatially resolved spectroscopy in probing the detailed kinematic properties of the stripped gas, which can provide important information for future simulations of RPS.

Key words: galaxies: clusters: intracluster medium – galaxies: evolution – galaxies: kinematics and dynamics – galaxies: individual: ESO 137-001 – techniques: imaging spectroscopy

1 INTRODUCTION

Galaxy clusters can accelerate the evolution of galaxies within them. The dense environment leads to gas deficiency in the cluster galaxies and drives these galaxies to be redder, more spheroidal, and less star forming than their counterparts in the field (e.g., Dressler 1980; Lewis et al. 2002; Boselli & Gavazzi 2006). Ram pressure stripping (RPS) is an important hydrodynamical mechanism responsible for the environmental effects of cluster galaxies evolution (e.g., Gunn & Gott 1972; Quilis et al. 2000; Boselli et al. 2022). As galaxies move in the hot ($T \sim 10^7 - 10^8$ K, $n_{\text{ICM}} \sim 10^{-4} - 10^{-2}$ cm⁻³) intracluster medium (ICM) (e.g., Sarazin 1986), the drag force from the ICM exerts the ram pressure on them. This pressure not only reorganizes the distribution and kinematic state of the interstellar medium (ISM),

but also strips it out from the galaxies, which can rapidly quench the star formation activity in a short time-scale ($\lesssim 1$ Gyr) (e.g., Roediger & Brügggen 2007; Boselli et al. 2008; Tonnesen & Bryan 2009; Fossati et al. 2018). A short-lived starburst can also occur in the galaxies during the RPS process, especially when the stripped ISM moves across the galaxy discs and creates instabilities/turbulence to help the collapse of the molecular clouds (e.g., Gavazzi et al. 1995; Bekki & Couch 2003; Lee et al. 2020; Boselli et al. 2021).

Besides its significant role in galaxy evolution, RPS can also influence the surrounding environment of galaxies through the stripped ISM. After being removed from the galaxies, the stripped ISM is able to get mixed with the ambient hot ICM. The cold gas can be heated, excited, and evaporated, which changes the phase of the stripped ISM and induce it to evolve as part of the ICM (e.g., Sun et al. 2022, see Boselli et al. 2022 for a review). Many of the ICM clumps are likely originated from the stripped cold gas, suggesting RPS can contribute to the inhomogeneity or clumpiness of the ICM (e.g., Vazza et al.

* E-mail: rongxinluo217@gmail.com

† E-mail: ms0071@uah.edu

2013; Ge et al. 2021). The stripped ISM can potentially enrich the ICM and modify its metallicity distribution, although the contribution is not significant as those from other mechanisms, such as the stellar evolution in the cluster galaxies, the stellar and AGN feedbacks (e.g., Schindler et al. 2005; Domainko et al. 2006; Kapferer et al. 2007). In addition, it is also known that some stripped ISM can form giant molecular clouds and turn into new stars, especially in the high-pressure environments, which may contribute to the intracluster light (see Boselli et al. 2022 for a review).

RPS events have been discovered in many nearby cluster galaxies, based on the multi-wavelength observations from radio, mm, IR, optical, UV, and X-ray (see Boselli et al. 2022 for a review). These studies present the important roles of RPS in gas removing and star formation quenching/triggering and highlight its effects on the evolution of cluster galaxies. In addition, these observations also reveal the multi-phase gas content in some spectacular stripped tails, which provides a great opportunity to study the evolution of stripped ISM and its mixing with the ICM.

ESO 137-001 is one of the nearest galaxies which are undergoing extreme RPS events and present clear multi-phase gas content in the stripped tails (Sun et al. 2006, 2007, 2010; Sivanandam et al. 2010; Jáchym et al. 2014). It is a late-type spiral galaxy in the Norma cluster (A3627; $R_A = 2$ Mpc, $M_{\text{dyn}} \sim 1 \times 10^{15} M_{\odot}$, $\sigma = 925$ km s^{-1}) and is located at a projected distance of ~ 200 kpc from the central cluster galaxy. Its line-of-sight (LOS) velocity (4680 ± 71 km s^{-1} ; Woudt et al. 2004) is close to the average LOS velocity of the cluster (4871 ± 54 km s^{-1} ; Woudt et al. 2008), suggesting this galaxy mainly moves on the plane of the sky. Based on the semi-analytic modeling of the possible orbits for ESO 137-001, Jáchym et al. (2014) suggested this galaxy is currently moving with a high velocity of ~ 3000 km s^{-1} and is located about 100 Myr before pericenter. The RPS tails of ESO 137-001 are first discovered with X-ray imaging from *Chandra* and *XMM-Newton* (Sun et al. 2006, 2010). The X-ray tails are stripped away from the cluster centre and extend to ~ 80 kpc projected distance from the galaxy. There are two narrow branches in the stripped tails, which contain a total mass of X-ray gas $\sim 10^9 M_{\odot}$. Following observations with optical imaging and spectroscopy reveal the $H\alpha$ emission from the bright H II regions and diffuse ionized gas in the stripped tails, which extend to ~ 40 kpc projected distance from the galaxy (Sun et al. 2007, 2010). Warm molecular gas was also detected to ~ 20 kpc along the stripped tails of ESO 137-001, with a total mass more than $10^7 M_{\odot}$ (Sivanandam et al. 2010). Based on the observations of *APEX* and *ALMA*, Jáchym et al. (2014, 2019) detected the CO(2-1) emission to ~ 60 kpc along the stripped tails and measured a total mass of cold molecular gas more than $\sim 10^9 M_{\odot}$.

Wide-field optical integral-field spectroscopy (IFS) has great potential to study the RPS process, since it can provide rich information about the detailed physical properties and kinematic structures of the ionized gas (i.e., warm phase) in the stripped tails (e.g., Merluzzi et al. 2013; Fumagalli et al. 2014; Fossati et al. 2016, 2019; Consolandi et al. 2017; Poggianti et al. 2017; Boselli et al. 2018; Liu et al. 2021), which is a key to explore the phase changing and evolution of the stripped ISM. Fumagalli et al. (2014) and Fossati et al. (2016) performed the *MUSE* observations to cover ESO 137-001 and the front part of its primary tail. Fumagalli et al. (2014) found the stripped ionized gas maintains the rotation imprint of the galaxy disc to ~ 20 kpc downstream that was first reported by Sun et al. (2010), and presents an enhancement of the velocity dispersion along the tails. Fossati et al. (2016) distinguished the diffuse ionized gas from the bright H II regions in the stripped tails and studied its excitation mechanism. They found the photoionization and shock ionization models cannot

Table 1. Properties of ESO 137-001

Heliocentric velocity (km s^{-1}) ^a	4647 (-224)
Offset (kpc) ^b	180
Position Angle	$\sim 9^\circ$
Inclination	$\sim 66^\circ$
M_{\star} ($10^9 M_{\odot}$) ^c	5-8
L_{FIR} ($10^9 L_{\odot}$) ^d	5.2
M_{mol} ($10^9 M_{\odot}$) ^e	~ 1.1
SFR ($M_{\odot} \text{ yr}^{-1}$) (Galaxy)	1.2
Tail length (kpc) ^f	80 - 87 (X-ray/ $H\alpha$)

Note:

Adopted from Waldron et al. (2023) to summarise the key properties of ESO 137-001 relative to this work.

(a) The heliocentric velocity of the galaxy is determined from the stellar spectrum around the nucleus (Section 2). The velocity value in parentheses is the radial velocity relative to that of Abell 3627 (Woudt et al. 2004).

(b) The projected offset of the galaxy from the X-ray centre of A3627.

(c) The total stellar mass estimated from Sun et al. (2010).

(d) The total FIR luminosity from the *Herschel* data (see details in Waldron et al. 2023).

(e) The total mass of the molecular gas in the galaxy from Jáchym et al. (2014).

(f) The full tail length.

explain the high values of the $[N \text{ II}]/H\alpha$ and $[O \text{ I}]/H\alpha$ observed in the diffuse ionized gas, suggesting other mechanisms (e.g., thermal conduction and magnetohydrodynamic waves, etc) may play a role in its excitation. As discussed above, ESO 137-001 has become the RPS galaxy with the richest amount of multi-wavelength data.

To further investigate the RPS process in ESO 137-001, we combine all the archival *MUSE* data with our own observations to complete the full coverage of the galaxy and its whole stripped tails. The map of $H\alpha$ surface brightness has been used in comparisons between the $H\alpha$ and X-ray emission from the diffuse gas in a large sample of RPS tails (Sun et al. 2022). This research reveals the connection between the warm and hot phases in the stripped ISM and provides evidence of its mixing with the ICM. In this paper, we focus on the kinematic properties of the ionized gas and study their variations in ESO 137-001 and its stripped tails. Details about the *MUSE* observations and data processing are described in Section 2. The kinematic maps of the ionized gas and the corresponding analyses of kernel density estimation are presented in Section 3. In addition, we also compare the motions of gas and stars in the galaxy disc and explore how the gas kinematics change along the stripped tails. Finally, discussion and conclusions follow in Section 4 and 5. Throughout this paper, we adopt the same distance and scale as used in Sun et al. (2010), a luminosity distance of 69.6 Mpc and $1'' = 0.327$ kpc. As described in Section 2, ESO 137-001's system velocity is fixed at 4647 km s^{-1} from its central stellar spectrum.

2 OBSERVATIONS AND DATA PROCESSING

We performed the *MUSE* (Multi-Unit Spectroscopic Explorer, Bacon et al. 2010) observations for ESO 137-001 with a wide-field mode through the European Southern Observatory (ESO) programs 095.A-0512(A) (PI: M. Sun) and 0104.A-0226(A) (PI: M. Sun). In addition, we also collect all the *MUSE* archive data from the ESO programs 60.A-9349(A) (Science Verification) and 60.A-9100(G) (Science Verification). The observational dates of these programs are from June 21, 2014 to March 17, 2020. The seeing changes from

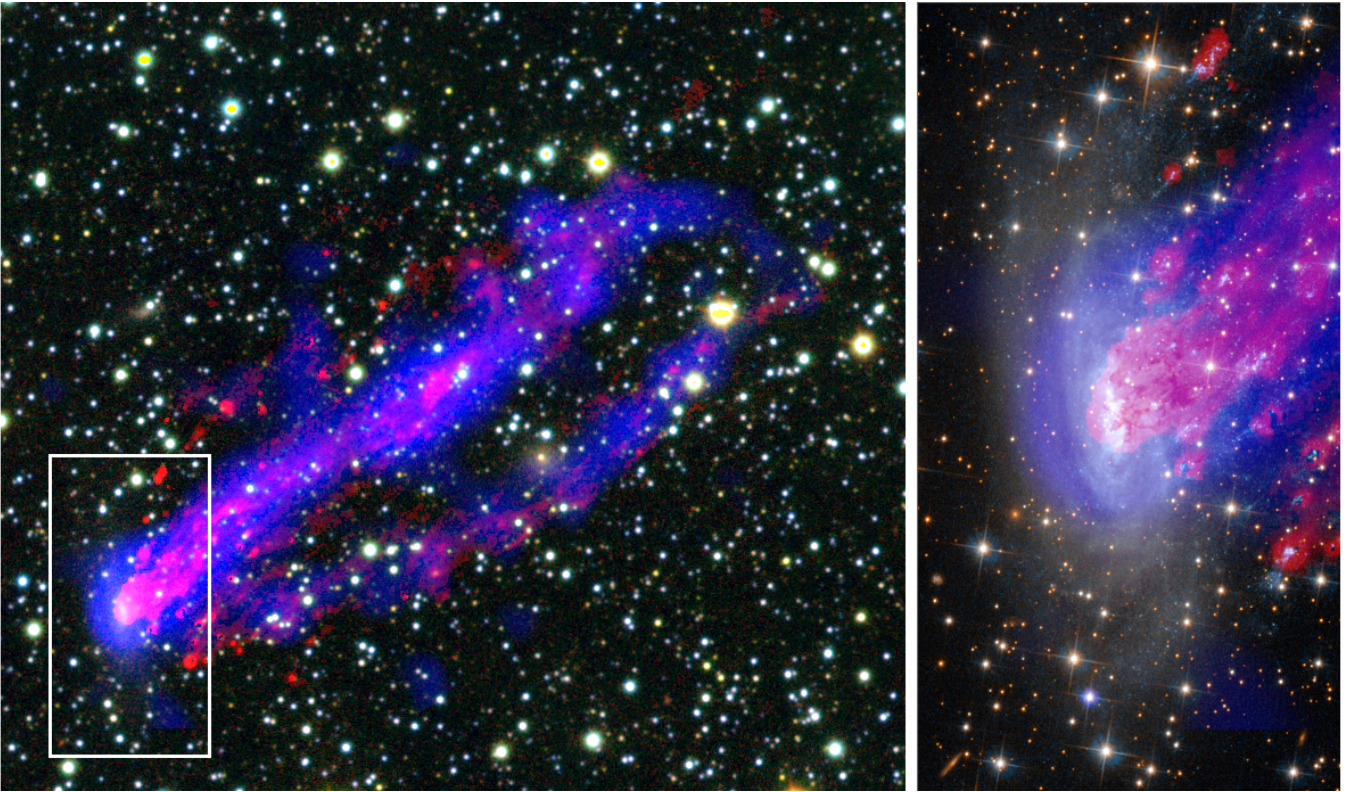


Figure 1. The composite images of ESO 137-001 and its stripped tails. Left panel: $H\alpha$ tails (red, from this work) and X-ray tails (blue, from *Chandra*, Sun et al. 2010) overlaid on the composite background of R, J, and Ks band images. The R band image is from the CTIO V. M. Blanco 4-m telescope, while the J and Ks band images are from VIRCAM. The white box shows the footprint of the *HST* image on the right. Right panel: *HST* image of the galaxy disc overlaid with the $H\alpha$ and X-ray tails (Credit of the *HST* image: ESA/Hubble²).

0'57 to 1'94 with a median of 1'04 and the airmass ranges from 1.24 to 1.60 with a median of 1.25. The total exposure time is 5 hours and 35 minutes. The detailed observational information is listed in Table 2. As shown in Fig. 2, we have a mosaic of 11 *MUSE* pointings to cover the main body of ESO 137-001 and its whole stripped tails. The wavelength coverage is 4750 - 9350 Å with a spectral resolution of $R \sim 2600$ at the wavelength of $H\alpha$ emission line. As discussed in Boselli et al. (2021), for the spectral resolution of *MUSE*, the uncertainty of velocity dispersion is large when it is lower than ~ 25 -30 km s^{-1} . Since our studies focus on the diffuse ionized gas in stripped tails which typically has velocity dispersion larger than 30 km s^{-1} , the above limit should not influence the results and conclusions in this paper.

For each pointing, we used the *MUSE* pipeline (version 2.8.1; Weilbacher et al. 2012, 2020) with the ESO Recipe Execution Tool (EsoRex; ESO CPL Development Team 2015) to reduce the raw data, which provides a standard procedure to calibrate the individual exposures and combine them into a datacube (see the *MUSE* pipeline manual³ for more details). Further sky subtraction was performed with the Zurich Atmosphere Purge software (ZAP; Soto et al. 2016), which involved principal component analysis to characterise the sky residuals remaining in the datacube and remove them. By using the CubeMosaic class implemented in the *MUSE* Python Data Analysis Framework (MPDAF) package (Bacon et al. 2016), we combined the individual datacubes into the final mosaic. In this process, the individual datacubes were first manually aligned by adopting the

bright 2MASS stars as a reference. Then, the 5σ -clipping average was performed on them to build the final datacube mosaic and remove the outliers. We also propagated the variance and write them into the final datacube mosaic.

Before the spectral analysis of the final datacube mosaic, we corrected the foreground Galactic extinction of data based on the colour excess from the dust map of Schlegel et al. (1998) with the recalibration of Schlafly & Finkbeiner (2011). The Galaxy extinction law from Fitzpatrick (1999) with $R_V = 3.1$ is adopted in the above correction. Given the faintness of the diffuse emission and the seeing value, a median filter with a kernel of 4×4 spaxels (or $0''.8 \times 0''.8$) was also chosen to smooth the final datacube mosaic. Then we adopted the public IDL software Kubeviz⁴ (Fossati et al. 2016) to fit each emission line with the Gaussian profile and derived the emission-line fluxes, the velocity and velocity dispersion of the ionized gas. The spaxels with signal-to-noise ratio (S/N) < 3 and velocity error and velocity dispersion error > 50 km s^{-1} were masked. In addition, we also masked the spaxels with extreme outliers in the distributions of velocity and velocity dispersion.

To measure the stellar kinematic properties in the galaxy disc and compare it with that of the ionized gas, we made a subcube to cover the D_{25} (the isophotal level of 25 mag arcsec^{-2} in the B band) of ESO 137-001. The subcube has a spatial size of $100'' \times 50''$ and the same wavelength range as the above datacube mosaic. We computed the S/N of the stellar continuum within the wavelength range of 5300 - 5500 Å and adopted the adaptive Voronoi method (Cappellari & Copin 2003) to spatially bin the data with a minimum S/N of 40.

² <https://esahubble.org/images/heic1404a/>

³ <https://www.eso.org/sci/software/pipelines/muse/>

⁴ <https://www.mpe.mpg.de/dwilman/kubeviz/Welcome.html>

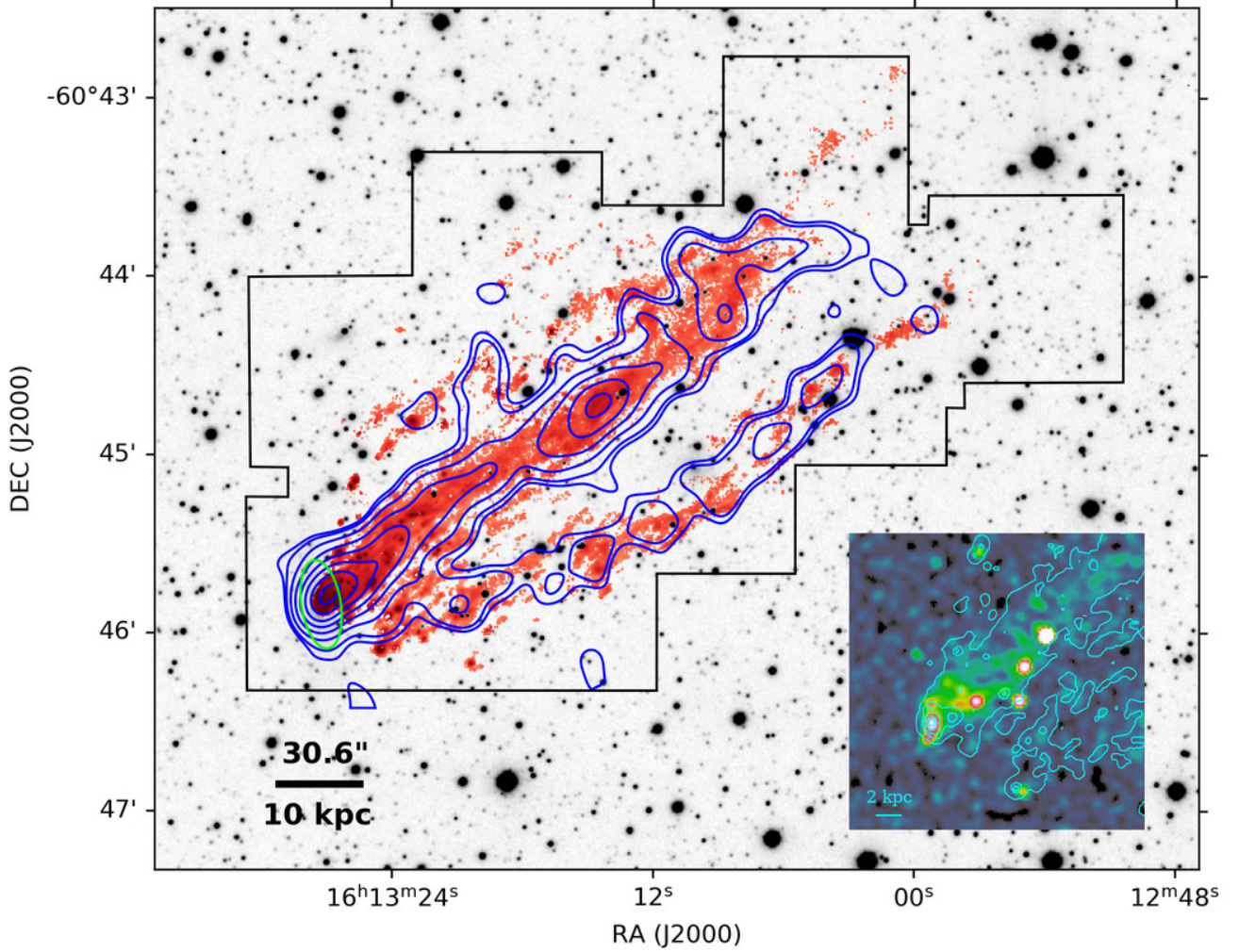


Figure 2. The J band image of ESO 137-001 and its stripped tails from *VIRCAM*. The FOV of 11 *MUSE* pointings is enclosed in the black lines and the detected $H\alpha$ emission is overlaid in red. The contours in blue show the X-ray emission observed by *Chandra* (Sun et al. 2010). The green ellipse shows the half-light radius of the galaxy from the *HST* F160W image. One can see the good positional correlation between the diffuse X-ray and $H\alpha$ emission. The X-ray stripping front and the $H\alpha$ stripping front are at the same position, as shown in the zoom-in inset (0.6 - 2 keV X-ray image + cyan $H\alpha$ contours). Note that the blue X-ray contours are from heavily smoothed X-ray image to enhance the faint, diffuse X-ray tail (see Fig. 1 of Sun et al. 2010) so the X-ray contours appear more extended than the $H\alpha$ emission but the X-ray - $H\alpha$ spatial correlation is well established in Sun et al. (2022).

Table 2. The observational blocks used for making the mosaic of ESO 137-001 and its stripped tails

OB	RA (hh mm ss)	Dec ($^{\circ}$ ' ")	Obs date	T_{exp} (s)	Airmass	Seeing (arcsec)	Program ID / PI
OB1	16 13 25.91	-60 44 31.3	February 6, 2020	720×2	1.532-1.583	1.87-1.94	0104.A-0226(A) / Sun
OB2-P1	16 13 24.70	-60 45 39.1	June 21, 2014	900×3	1.239-1.251	0.83-0.96	60.A-9349(A) / SV
OB2-P2	16 13 17.69	-60 44 48.9	June 21, 2014	900	1.238	0.78	60.A-9349(A) / SV
OB3	16 13 24.25	-60 45 45.8	June 18, 2017	900×3	1.238-1.251	0.80-1.21	60.A-9100(G) / SV
OB4	16 13 18.45	-60 43 49.0	February 4, 2020	720×2	1.540-1.593	1.11-1.25	0104.A-0226(A) / Sun
OB5	16 13 16.54	-60 45 44.3	May 20, 2015	1050×2	1.238-1.243	1.22-1.35	095.A-0512(A) / Sun
OB6	16 13 10.10	-60 44 07.9	May 21, 2015	1049×2	1.238-1.241	1.52-1.88	095.A-0512(A) / Sun
OB7-P1	16 13 10.09	-60 45 06.9	May 21, 2015	900×2	1.347-1.380	0.81-1.00	095.A-0512(A) / Sun
OB7-P2	16 13 02.12	-60 44 20.8	May 21, 2015	627×2	1.418-1.451	1.04-1.12	095.A-0512(A) / Sun
OB8	16 13 04.45	-60 43 15.6	February 5, 2020	720×2	1.549-1.602	0.96-0.97	0104.A-0226(A) / Sun
OB9	16 12 54.88	-60 44 01.9	March 17, 2020	720×2	1.238-1.240	0.57-0.71	0104.A-0226(A) / Sun

Note: The observational blocks are ordered in right ascension from the East to the West. The OB2 and OB7 both include two pointings. The previous works on ESO 137-001 (Fumagalli et al. 2014; Fossati et al. 2016) only used the data from 60.A-9349(A) to cover the galaxy and the front part of the primary tail. SV stands for Science Verification.

Then we use the software pPXF (Cappellari & Emsellem 2004; Cappellari 2017) to fit the continuum and measure the stellar velocity and velocity dispersion for each bin. The continuum was modeled with the templates selected from the E-MILES simple stellar population models⁵ (Vazdekis et al. 2016), which are generated with a Chabrier (2003) initial mass function and BaSTI isochrones (Pietrinferni et al. 2004). A total of 32 stellar templates were adopted, with eight ages increasing from 0.15 to 14 Gyr and four metallicities $[M/H]$ ranging from -1.49 to 0.40. To avoid the sky residuals in the red part of *MUSE* spectra, we limited the wavelength range within 4800 - 7000 Å in the fitting process. We also extracted the integrated spectra within an aperture of 3'' diameter and measured the system velocity of ESO 137-001 based on the stellar kinematics. The obtained system velocity is $4647 \pm 5 \text{ km s}^{-1}$, which is adopted as the velocity reference of the stars and ionized gas throughout the paper.

3 RESULTS

3.1 Overall distribution and kinematics of the ionized gas

In Fig. 3, we present the two-dimensional maps of the $H\alpha$ surface brightness (corrected for the Galactic extinction) and S/N, the velocity, and the velocity dispersion of the ionized gas in ESO 137-001 and its stripped tails. Our *MUSE* observations provide a limit of $1.6 \times 10^{-18} \text{ erg s}^{-1} \text{ cm}^{-2} \text{ arcsec}^{-2}$ for the $H\alpha$ surface brightness at $S/N > 3$, enabling us to trace the detailed distribution and structures of the ionized gas across the whole stripped tails. Based on the $H\alpha$ surface brightness, we separated H II regions and the diffuse ionized gas⁶ in the stripped tails. The details for the identification of H II regions were presented in Waldron et al. (2023). In brief, we first adopted SExtractor with criteria on the shape of regions to identify the H II region candidates. Then we applied the limits on the integrated $H\alpha$ flux and $[N \text{ II}]/H\alpha$ emission-line ratio to select the final H II regions. In total, we selected 43 H II regions in the stripped tails. They have a median $H\alpha$ surface brightness of $9.4 \times 10^{-17} \text{ erg s}^{-1} \text{ cm}^{-2} \text{ arcsec}^{-2}$, which is significantly higher than that of $1.4 \times 10^{-17} \text{ erg s}^{-1} \text{ cm}^{-2} \text{ arcsec}^{-2}$ for the diffuse ionized gas. All H II regions are located within the inner half of the stripped tails and have a median projected distance of $\sim 11 \text{ kpc}$ from the galaxy centre, suggesting their distributions tend to be close to the galaxy disc. This signature has also been noticed in the previous studies with the narrow band imaging and IFS observations (Sun et al. 2007; Fossati et al. 2016). At the middle part of the stripped tails ($\sim 40 \text{ kpc}$ projected distance from the galaxy centre), one region with diffuse ionized gas also presents bright $H\alpha$ emission. As shown in (Sun et al. 2022), this region also has the highest X-ray surface brightness in the tail. There are no significant kinematic differences between this bright blob and its surrounding diffuse gas, suggesting it is just a denser concentration of gas with respect to the surrounding regions.

The stripped tails of ESO 137-001 are extended along the direction with a position angle (PA) of $\sim -54^\circ$ (from the North, “-” for clockwise) and split into three main structures, including the central

tail, the southern tail, and the northern tail. The central tail is the most extended and spread structure with a good continuity, which has an average width of $\sim 10 \text{ kpc}$ and reaches to $\sim 87 \text{ kpc}$ projected distance from the galaxy centre (16:13:27.231, -60:45:50.60) (The centre position was determined from the peaks of the X-ray, $H\alpha$ and CO emission in ESO 137-001, as well as the GALFIT fit to the *HST* images, see Waldron et al. 2023). The southern tail also extends to $\sim 75 \text{ kpc}$ projected distance from the galaxy centre, while its average width is only $\sim 5 \text{ kpc}$ and the tail is not as continuous as the central tail. On the contrary, the northern tail is rather fragmented and presents several filamentary substructures. This tail covers a region of $\sim 5 \text{ kpc} \times 40 \text{ kpc}$. The central tail is still connected with the inner galaxy disc while the northern and southern tails are not connected with it, suggesting they are probably at different stripping stages.

The velocity field of ionized gas presents a velocity gradient through the inner half of the stripped tails in ESO 137-001. From the northern tail to the southern tail, the LOS velocity of the ionized gas changes from blueshifted to redshifted and its median value ranges from $\sim -80 \text{ km s}^{-1}$ to $\sim 120 \text{ km s}^{-1}$. This velocity pattern has also been observed by the spectroscopy of individual H II regions (Sun et al. 2010) and the previous IFS study (Fumagalli et al. 2014), which is considered as the rotation imprint of the galaxy disc. Beyond the inner half, the velocity field in the remaining part of the stripped tails becomes more disordered, indicating the kinematics state of the ionized gas could be different between these two regions. The velocity dispersion of ionized gas has a median value of $\sim 30 \text{ km s}^{-1}$ in the galaxy disc and H II regions, while the diffuse ionized gas in the stripped tails presents an enhanced velocity dispersion to a median value of $\sim 80 \text{ km s}^{-1}$, suggesting it is probably more turbulent. Considering this kinematic difference between the H II regions and diffuse ionized gas, we excluded H II regions from the analysis in the rest of this section and Section 3.3. Note that several discrete regions with high velocity dispersion are elongated along the extension direction of the stripped tails and associated with kinematically distinct filamentary features in the velocity field. These may be distinct filamentary entities in the tails that are projected along the same LOS as other components, inducing the blending of emission lines with different velocities and yielding large values of velocity dispersion. For the regions with velocity dispersion higher than 150 km s^{-1} , more than 80% of them show the double-peak or non-Gaussian profiles for the emission lines. These regions only include less than 6% spaxels of the whole datacube, which will not affect the following kinematic analysis.

We adopted the kernel density estimation to show the distributions of velocity and the velocity dispersion of the ionized gas in ESO 137-001 and its stripped tails. Kernel density estimation is a non-parametric way to estimate the probability density function, which allows us to visualize the underlying distribution of the variables in large datasets. We present both the $H\alpha$ flux weighted and unweighted results. In general, the flux-weighted results show more concentrated distributions than the unweighted ones. Our conclusions are based on the flux-weighted results, while we also keep the unweighted results as a reference for the general distribution of the data, especially faint regions. As shown in Fig. 4, the velocity of most ionized gas ranges from $\sim -100 \text{ km s}^{-1}$ to $\sim 150 \text{ km s}^{-1}$, while their velocity dispersion is mainly within 120 km s^{-1} . In Fig. 5, we also present the kernel density estimation for the velocity and velocity dispersion of the ionized gas vs. the distance along the stripped tails. The estimation was performed in eleven individual regions with a direction parallel to the major axis of the galaxy. While we adopted $\sim 8 \text{ kpc}$ as the width of the first region to cover the galaxy disc, the width of the regions along the stripped tails was set as $\sim 6.5 \text{ kpc}$.

⁵ <http://research.iac.es/proyecto/miles/pages/spectral-energy-distributions-seeds/e-miles.php>

⁶ In the stripped tails, the ionized gas outside H II regions is considered as the diffuse ionized gas. This could be different from the original concept of the diffuse ionized gas (DIG), which represents the diffuse ionized interstellar medium in the galaxy discs or haloes. The diffuse ionized gas in the stripped tails also includes the mixing component of the stripped ISM and the surrounding ICM.

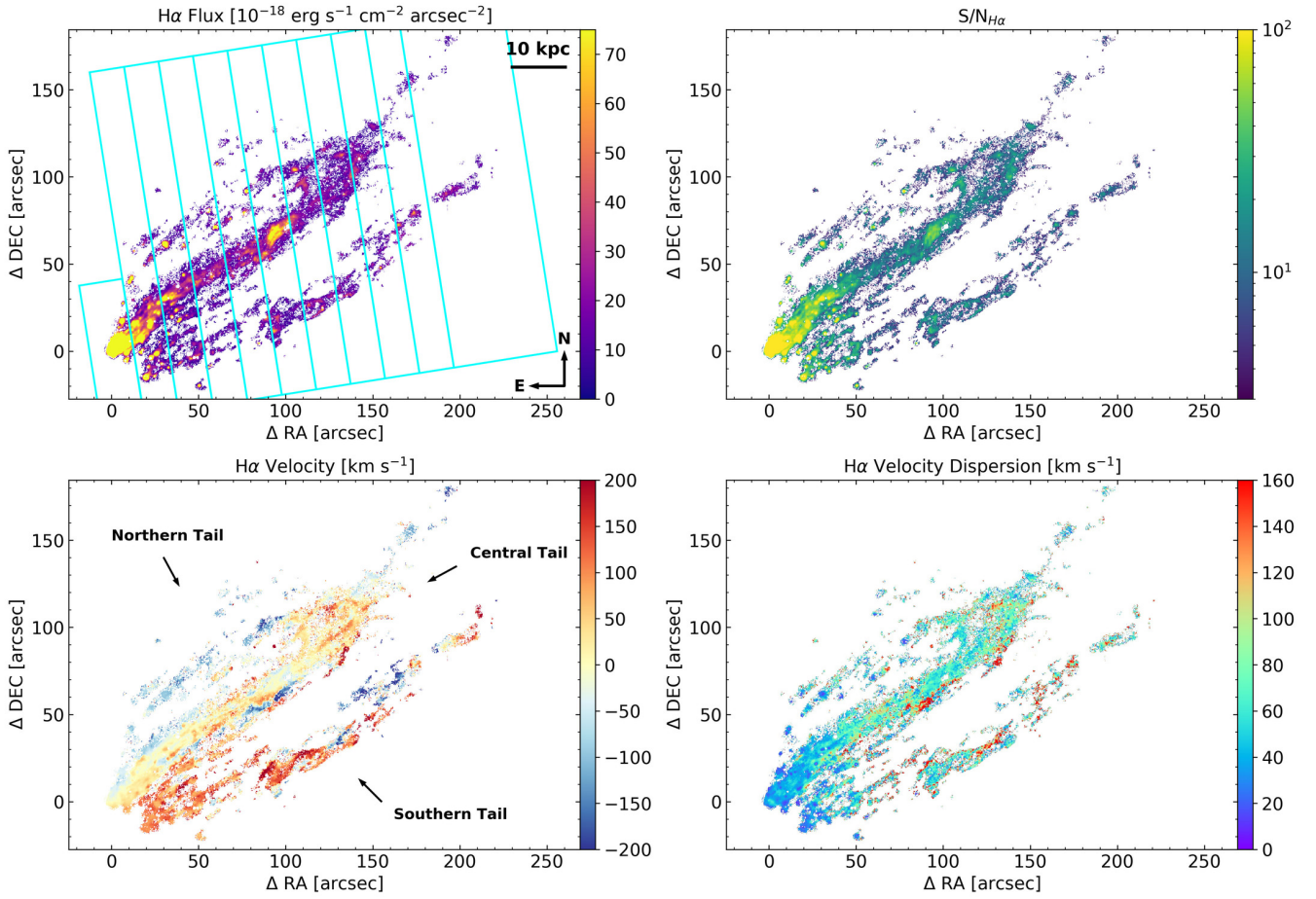


Figure 3. Two-dimensional maps for the properties of the ionized gas in ESO 137-001 and its stripped tails, including the $H\alpha$ surface brightness and S/N , the velocity, and the velocity dispersion. The cyan boxes show the eleven regions where we performed the kernel density estimation. The major axis of each region is paralleled with the major axis of the galaxy. The central tail, the southern tail, and the northern tail are marked in the gas velocity field.

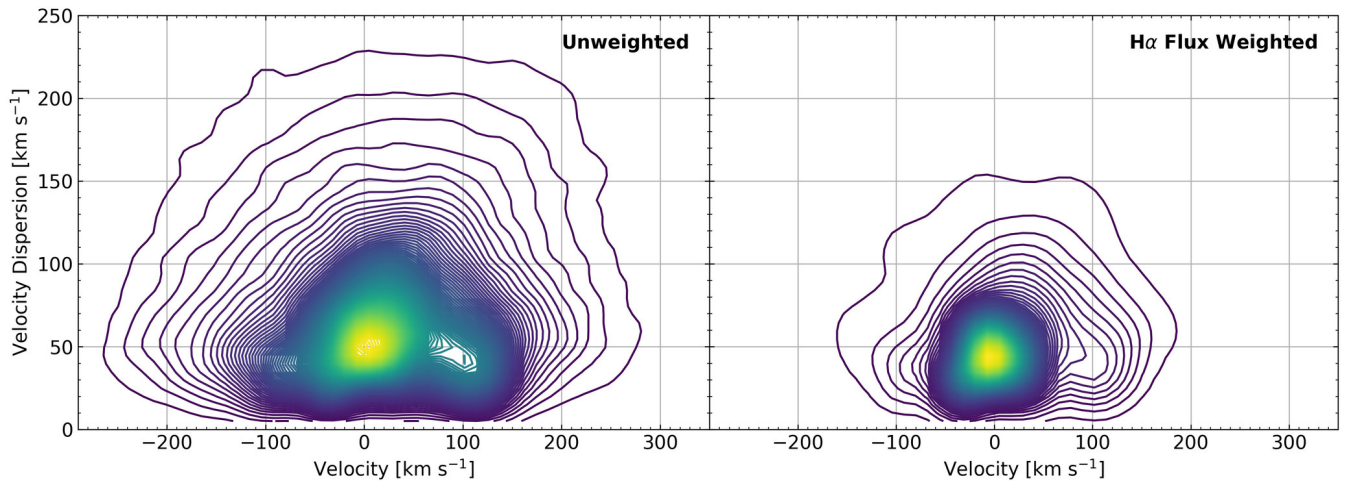


Figure 4. The kernel density estimation for the velocity vs. the velocity dispersion of the ionized gas in ESO 137-001 and its stripped tails. The contours are separated by 1%. The median velocity and velocity dispersion are 17.3 km s^{-1} and 62.5 km s^{-1} respectively for unweighted, and 0.4 km s^{-1} and 48.3 km s^{-1} respectively for weighted.

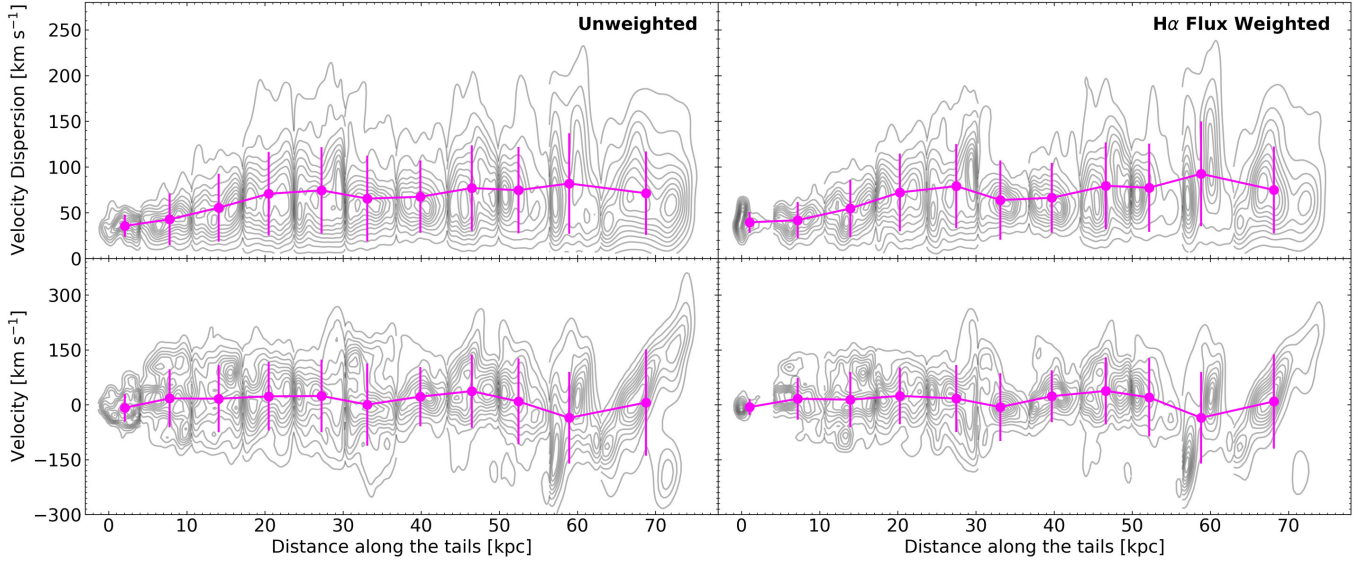


Figure 5. The kernel density estimation for the velocity and the velocity dispersion of the ionized gas vs. the distance along the stripped tails. The contours are separated by 10%. The magenta dots show the median values ± 1 sigma scatter of the velocity and velocity dispersion in each region. The median velocities are $-8.3, 17.4, 16.5, 23.0, 24.0, 0.4, 22.2, 37.2, 9.0, -35.8$ and 6.1 km s^{-1} (in the order of distance, from small to large) for unweighted, and $-6.4, 16.4, 13.9, 24.2, 16.9, -6.3, 23.4, 37.9, 20.0, -35.6$ and 9.0 km s^{-1} for weighted, which suggests that most of the galaxy motion is on the plane of the sky.

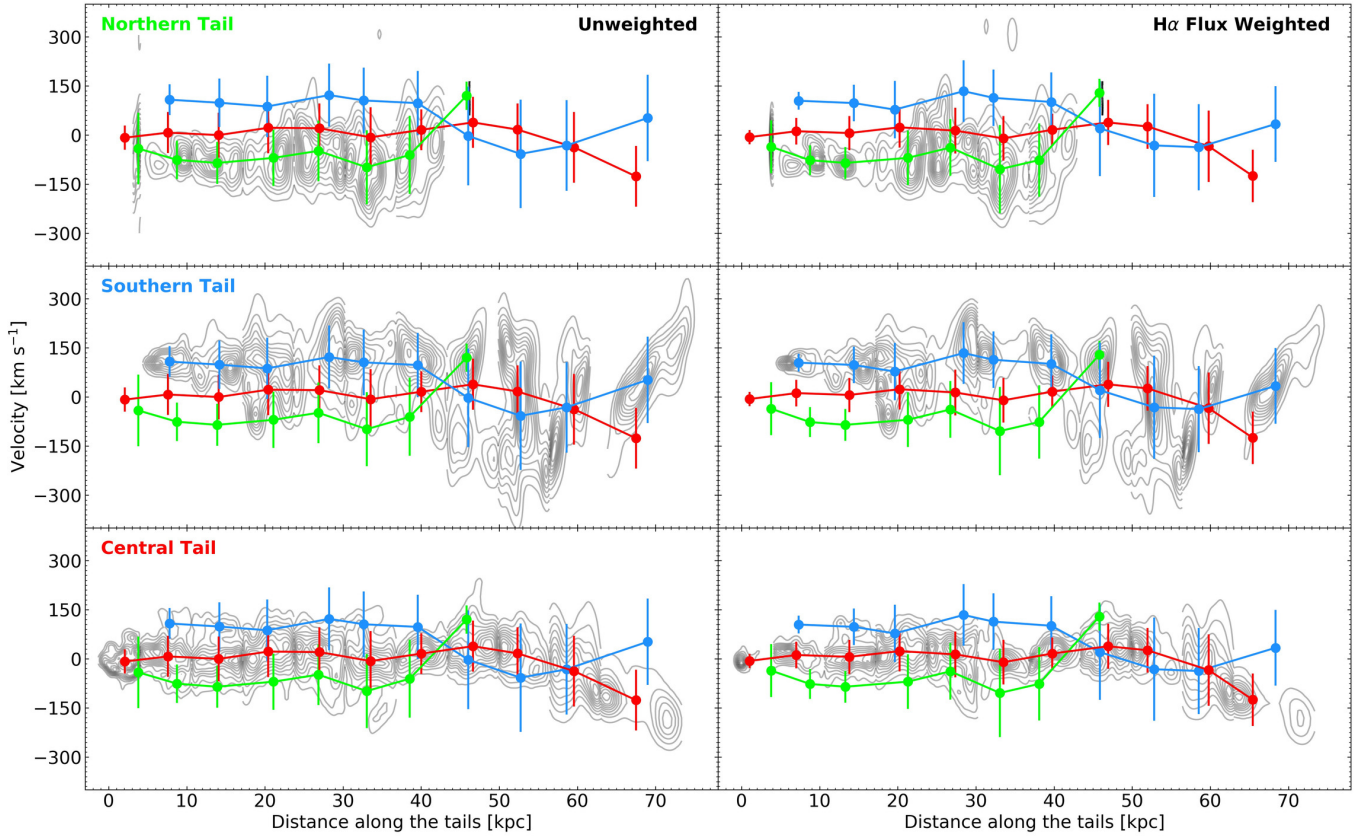


Figure 6. The kernel density estimation for the velocity of the ionized gas in three individual tails vs. the distance along the stripped tails. The contours are separated by 10%. The red, blue, and green dots show the median values ± 1 sigma bars of the velocity in each region from the central, the southern, and the northern tail, respectively. The three, initially kinematically distinct tails end with similar velocities at distance > 45 kpc.

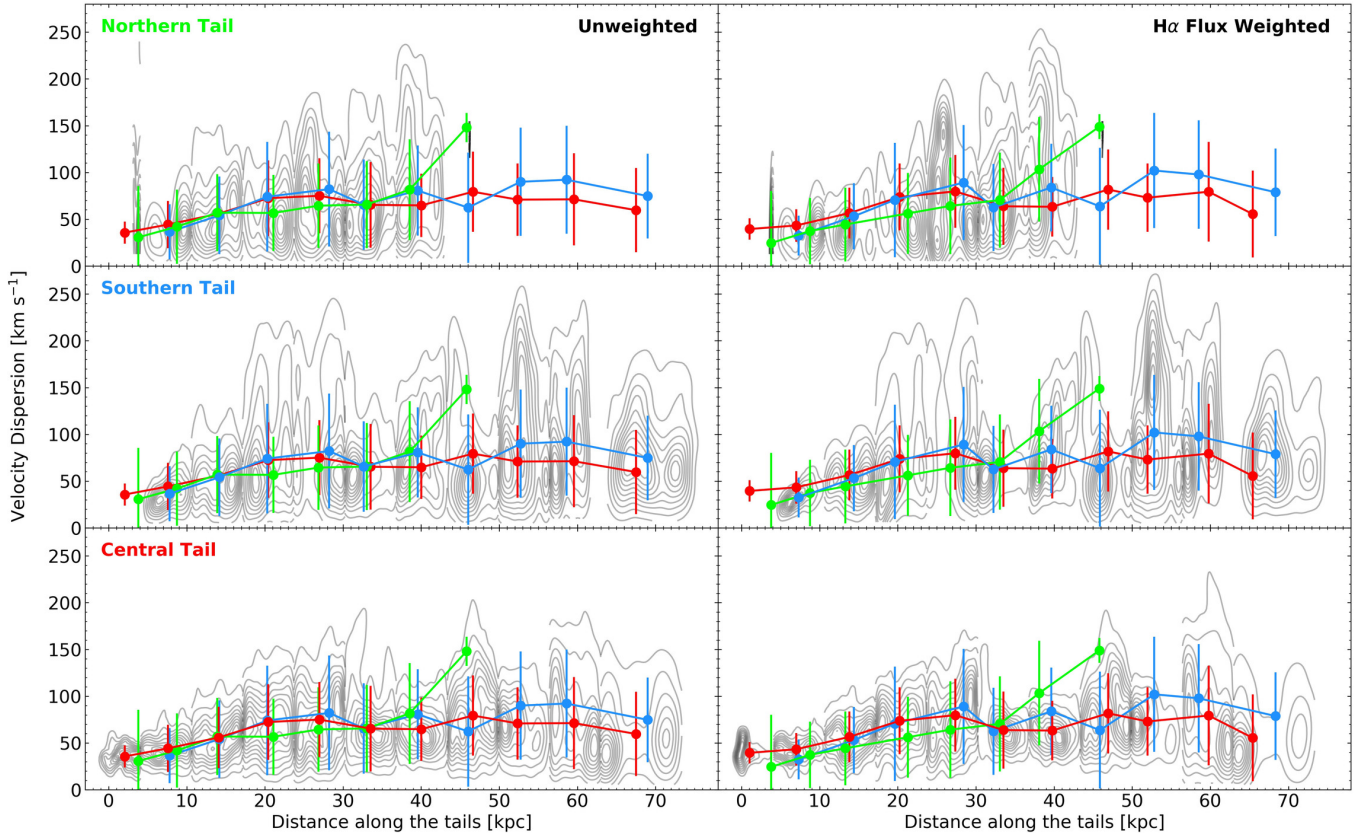


Figure 7. The kernel density estimation for the velocity dispersion of the ionized gas in each tail vs. the distance along the stripped tails. The contours are separated by 10%. The red, blue, and green dots show the median values ± 1 sigma bars of the velocity dispersion in each region from the central, the southern, and the northern tail, respectively.

For the last region, we used ~ 20 kpc as its width to collect enough data points. The exact positions of these regions are shown as cyan boxes in Fig. 3. The median velocity of the ionized gas in the stripped tails does not significantly change with the distance, which is around 15 km s^{-1} . This result confirms that the motion of ESO 137-001 is mainly on the sky plane, which has also been mentioned by several previous studies (Sun et al. 2006, 2007, 2010; Fumagalli et al. 2014; Jáchym et al. 2019). In addition, the small redshifted median velocity suggests that ESO 137-001 is also slightly moving towards us along the LOS. This is consistent with the implication from the radial velocity of ESO 137-001, which is $\sim 224 \text{ km s}^{-1}$ smaller than the Norma cluster’s velocity. The velocity spread of ionized gas is $\sim 350 \text{ km s}^{-1}$ in the stripped tails, which is significantly larger than that of $\sim 120 \text{ km s}^{-1}$ in the galaxy disc. While this result is generally consistent with the behaviours predicted by the simulations (e.g. Roediger & Brüggén 2008), the small fluctuations of velocity spread along the tails do not suggest strong turbulence there. The median velocity dispersion of ionized gas changes from $\sim 35 \text{ km s}^{-1}$ in the galaxy disc to $\sim 80 \text{ km s}^{-1}$ at ~ 20 kpc downstream and maintain a similar level in the remaining part of the stripped tails. The spread of velocity dispersion also presents a similar behaviour, which increases from $\sim 50 \text{ km s}^{-1}$ in the galaxy disc to $\sim 200 \text{ km s}^{-1}$ beyond ~ 20 kpc downstream of the stripped tails. These results suggest that the degree of turbulence in the diffuse ionized gas is probably enhanced from the galaxy disc to ~ 20 kpc along the stripped tails.

To further explore the kinematic differences between the three split tails, we performed similar kernel density estimations as above for each of them. The results are shown in Fig. 6 and 7. Within ~ 40

kpc, the three tails maintain distinctive velocities at $\sim -80 \text{ km s}^{-1}$ to $\sim 120 \text{ km s}^{-1}$, which further clearly shows the impact of the galactic rotation on the front part of the tails. Beyond the distance of ~ 40 kpc, the median velocity of ionized gas in different tails becomes about the same, indicating the disappearance of the velocity gradient. The median velocity dispersion of ionized gas in different tails presents a similar behaviour as that in Fig. 5, further supporting the enhanced degree of turbulence from the galaxy disc to ~ 20 kpc along the stripped tails. In addition, the spreads of the velocity and velocity dispersion of the ionized gas are also comparable in different tails. These results suggest that the general kinematic states of the ionized gas in three split tails are probably similar, except for the pattern of the velocity gradient across them. Note that different calculations of the distance and the direction of regions do not significantly affect the results of the above kernel density estimations. We have performed these analyses based on different definitions of the distance (e.g., the distance to the galaxy centre/major axis) or different directions of the regions (e.g., the major axes of the regions perpendicular to the extension direction of the stripped tails). The general kinematic behaviours of the ionized gas are similar to the above one in each case.

3.2 The distributions and velocity fields of the ionized gas and stars in the galaxy disc

To understand the state of ionized gas in the galaxy disc of ESO 137-001, we compared its distribution and velocity field with those of the stars. As shown in Fig. 9, the stars are well distributed in a disc

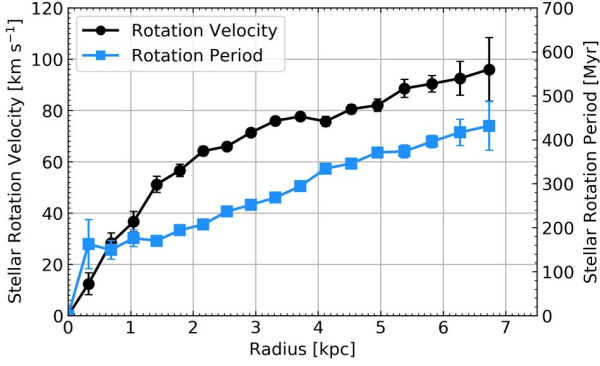


Figure 8. The stellar rotation curve of ESO 137-001 and the corresponding stellar rotation periods as a function of the radius.

shape and present a regular rotation motion. To measure the rotation curve of the stars, we adopted the tilted-ring method (e.g. Rogstad et al. 1974; Bosma 1978; Begeman 1987; Schoenmakers et al. 1997; Wong et al. 2004; Krajnović et al. 2006) to fit the stellar velocity field. In this method, the projected galaxy disc is divided into a set of elliptical annuli. For each annulus, the LOS velocity is fitted as a Fourier series, which describes the kinematic components with different azimuthal symmetries:

$$V_{\text{LOS}}(R, \psi) = V_{\text{sys}} + \sum_{n=1}^k [c_n(R)\sin(n\psi) + s_n(R)\cos(n\psi)]. \quad (1)$$

(R, ψ) represent the polar coordinate in the plane of the galaxy disc. V_{sys} is the system velocity of the galaxy. The first-order terms $c_1(R)\sin\psi$ and $s_1(R)\cos\psi$ describe the radial and rotational velocity components, while the higher-order terms could be related to the perturbations of gravitational potential (e.g., Schoenmakers et al. 1997; Wong et al. 2004; Krajnović et al. 2006). Thus, the stellar rotation curve can be derived as:

$$V_{\text{rot}}(R) = s_1(R)/\sin i, \quad (2)$$

where i is the inclination of the galaxy.

We used the software package Kinemetry (Krajnović et al. 2006) to fit the LOS velocity with a three-order Fourier series. The PAs and inclinations of the elliptical annuli are fixed at 9° and 66° , which are obtained with the photometric analysis of the *HST* images (Waldron et al. 2023). The galaxy centre was fixed at (16:13:27.231, -60:45:50.60) (see Section 3.1) and we adopted the system velocity derived in Section 2. The radial distribution of s_1 coefficient was used to derive the stellar rotation curve, which is shown in Fig. 8. Because of the limited S/N of the observed continuum spectra, we can only measure the stellar rotation velocity up to the radius of ~ 6.7 kpc. Based on the rotation curve, we also calculate the corresponding stellar rotation periods as a function of the radius (Fig. 8).

In Fig. 9, we present the velocity fields of the ionized gas and stars in the galaxy disc and make a comparison between them. The overall size of the ionized gas in the galaxy is drastically decreased, suggesting most gas component in the outer galaxy disc has been stripped. Ram pressure shapes the remnant ionized gas into a narrow cone, which connects the inner galaxy disc with the central tail. This connection indicates that the ionized gas in the inner galaxy disc could be the origin of the central tail and still feed the stripping process there. To clearly present the kinematic difference, we further calculate the error-weighted averages of the velocity differences between the ionized gas and stars in three regions across the galaxy disc. As shown in Fig. 10, there is an increasing of the velocity difference from ~ 0

km s^{-1} in the inner galaxy disc to $\sim 40 \text{ km s}^{-1}$ in the outer galaxy disc. Considering the galaxy has a small velocity component towards us, this redshifted velocity difference provides a potential hint of the gas deceleration due to the RPS. The above significant difference between the ionized gas and stars suggests the intense perturbations produced by the RPS and this process is already well advanced.

Numerical simulations have predicted the influence of RPS on the gas kinematics of galaxies, which includes changing the rotation curves, producing the mismatch between the kinematic centres of stars and gas components, unwinding the spiral arms, and inducing distortions in the velocity fields (e.g., Kronberger et al. 2008; Haan & Braun 2014; Bellhouse et al. 2021). Regarding observational studies, spatially-resolved spectroscopy can provide the detailed kinematic properties of RPS galaxies, which have shown several examples of the above effects. For the RPS galaxy SOS 114372, Merluzzi et al. (2013) observed the one-sided extraplanar ionized gas presents the rotation motion up to a projected distance of ~ 13 kpc from the galaxy disc, while the distribution and kinematics of the stars are symmetric and regular. Based on the *MUSE* and Fabry-Perot observations of galaxy IC 3476, Boselli et al. (2021) discovered the kinematic centre of the ionized gas has an offset of ~ 500 pc from that of the stars, due to the perturbations induced by the RPS process. In addition, they also found that the mean velocity of the gas with respect to that of the stars has been changed by $\sim 20 \text{ km s}^{-1}$. As shown in the GASP survey, the perturbations of velocity fields have also been observed in the ionized gas of several RPS galaxies, for example, J201 and J204 (e.g., Bellhouse et al. 2017; Gullieuszik et al. 2017).

The comparison between ESO 137-001 and the above targets indicates more intense effects of RPS on the gas kinematics of this galaxy, since the gas in the outer disc of ESO 137-001 has been fully removed while the loss of the gas content in other galaxies is relatively mild. The influence of RPS on gas kinematics depends on several factors, including the mass of the gas content, the gravitational potential of the RPS galaxy, the strength of the ram pressure, the geometrical configuration, and the stage of the stripping process. Both face-on and edge-on stripping processes exist in these galaxies, suggesting the geometrical configuration is not a key factor. In addition, the gas and stellar mass of ESO 137-001 are not outstanding among these galaxies. We thus propose the strength of the ram pressure and the stage of the stripping process may play important roles in shaping the intense RPS effects of ESO 137-001.

3.3 Modelling the velocity field of the ionized gas

To further quantify the kinematic state of the stripped tails in ESO 137-001 and the development of turbulence in the stripped gas, the velocity gradient from the galactic rotation needs to be first modeled and removed. As the galactic rotation imprint began to disappear as a function of the distance to the galaxy, the velocity field of the stripped gas is more at the mercy of turbulence in the wake. We constructed the velocity model for the residual galactic rotation based on the velocity gradient of the ionized gas. Since the kinematic properties of the ionized gas are not uniform along the stripped tails, we attempted two different methods: (1) select the front part of the tails with a clear velocity gradient and use it as the global velocity gradient; (2) divide the stripped tails into some regions along the tails and measure the velocity gradient in each region separately.

3.3.1 Modelling based on the global velocity gradient

As shown in Fig. 11, to derive the global velocity gradient, we selected the region including the head and inner half of ESO 137-001's

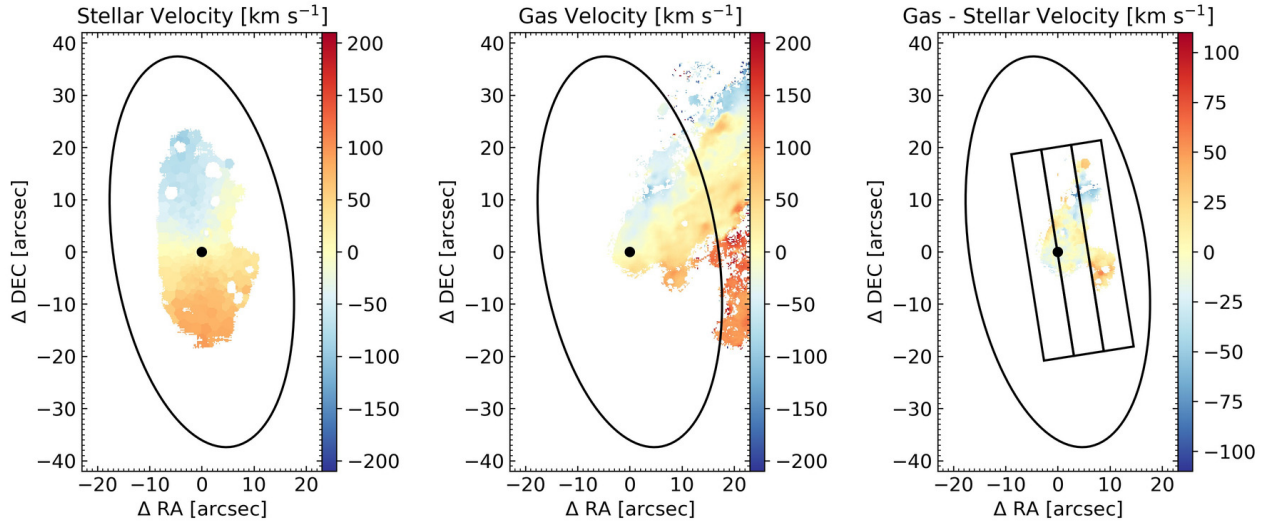


Figure 9. The comparison between the distributions and velocity fields of the ionized gas and stars in the galaxy disc of ESO 137-001. The foreground stars are masked in the stellar velocity field. The position of the galaxy centre is marked as the black circle. The black ellipses present the D_{25} of the galaxy. The black boxes show the three regions where we calculate the error-weighted averages of the velocity differences between the ionized gas and stars. The major axes of these regions are paralleled with the major axis of the galaxy. When the gas is decelerated by ram pressure, it is expected that gas should have a higher radial velocity than the galaxy, as indeed observed here.

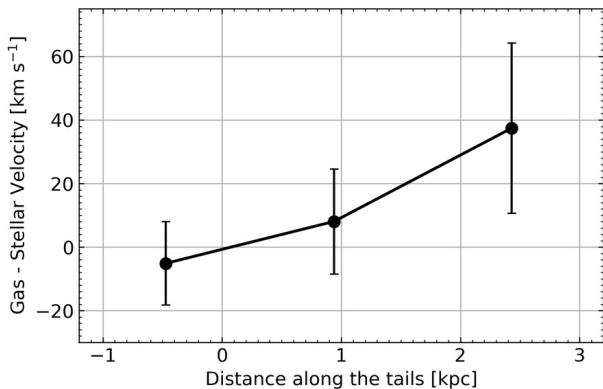


Figure 10. The error-weighted averages of the velocity differences between the ionized gas and stars as a function of the distance along the stripped tails. These averages are calculated in three regions across the galaxy disc, which are shown with black boxes in the right panel of Fig. 9.

stripped tails (within ~ 40 kpc from the major axis of the galaxy disc). To determine the best-fitting direction and slope of the global velocity gradient, we rotated the velocity field within the selected region at different angles and correspondingly calculated the $H\alpha$ flux-weighted averages of the velocities from the spaxels in each column. For each rotation angle, the velocity gradient was obtained by fitting the above average velocities as a function of the distance across the stripped tails. We adopted a piecewise function including a linear function and two plateaus as the fitting function (see the right panel of Fig. 11). Due to the statistical fluctuations in the data, the error-weighted averages in twenty-five distance bins were used in the fitting process. The best-fitting direction of the global velocity gradient was determined to have the lowest root mean square (RMS) in the corresponding residual velocity field (velocity field – velocity gradient), which is along the direction with a PA of $42 \pm 1^\circ$. The best-fitting slope of the global velocity gradient is $11.1 \pm 1.1 \text{ km s}^{-1} \text{ kpc}^{-1}$ between -74.9 km s^{-1} and 96.0 km s^{-1} at the distance of -6.2 kpc and 9.2 kpc. The velocity range of this gradient is generally con-

sistent with that of the stellar rotation curve, which further confirms it is the rotation imprint of the galaxy. For the whole velocity field, we obtained the model by applying the above velocity gradient to the rest of the stripped tails.

A possible caveat in the above analysis is that the fitting function might be too simple to well describe the gas velocity field. Our aim to fit the gas velocity field is to quantify the large-scale velocity gradient across the stripped tails. The choice of fitting function is based on the fact that this large-scale velocity gradient itself can be described as a linear function. On the other hand, there is no exact model for the large-scale velocity gradient across the stripped tails. In this case, the linear function could be a realistic description of a velocity gradient. On the small scale, the velocity fluctuations always exist in the turbulent environment of stripped tails. A more complicated function can exactly quantify these small-scale velocity fluctuations. However, this deviates from our research goal to quantify the large-scale velocity gradient.

Fig. 12 presents the velocity field model and its corresponding residual velocity field. While the rotation imprint is well removed in the front part of the stripped tails (or where the model is constructed), the residual velocity significantly increases in the rear half of the stripped tails. To quantitatively examine the velocity field model, we performed the kernel density estimation for the residual velocity vs. the distance along the stripped tails. The estimation was carried out in the same regions as defined in Section 3.1. As shown in Fig. 13 and 14, the median values of the residual velocity are close to zero within the inner ~ 40 kpc, indicating the global velocity gradient of the ionized gas has been well modeled and subtracted from the observed velocity field. There is still considerable residual velocity beyond the distance of ~ 40 kpc, presumably because the residual rotation no longer dominates the kinematics of the ionized gas there, while other motions such as turbulence may begin to play a role.

The kinematics of stripped tails are closely related to the original kinematic state of the ISM in galaxy discs and the effects of RPS. Since ESO 137-001 is a late-type spiral galaxy, the kinematics of the ionized gas in the galaxy disc should generally follow the stellar kinematics there. While the direction of the global velocity gradient

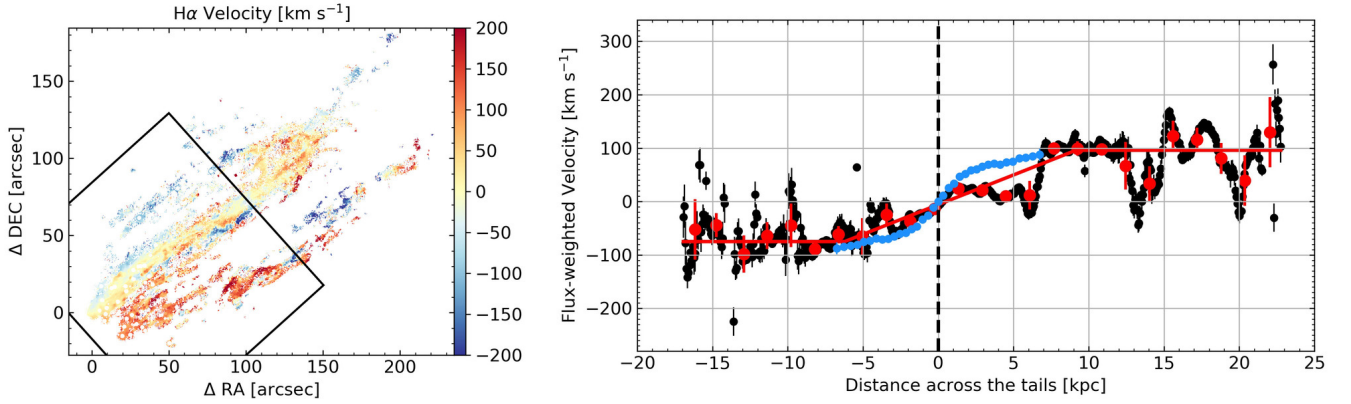


Figure 11. Fitting the global velocity gradient of the ionized gas in the stripped tails of ESO 137-001. Left panel: The velocity field of the ionized gas. The selected region with a clear velocity gradient is marked by the black box. Right panel: The black dots show the averaged velocities, weighted by the H α flux from spaxels in each column, while their error-weighted averages in twenty-five distance bins are presented in red dots. The red solid line describes the best-fitting global velocity gradient. The blue dots present the stellar rotation curve of the galaxy (without the projection correction). The position of the galaxy centre is indicated with the black dashed line.

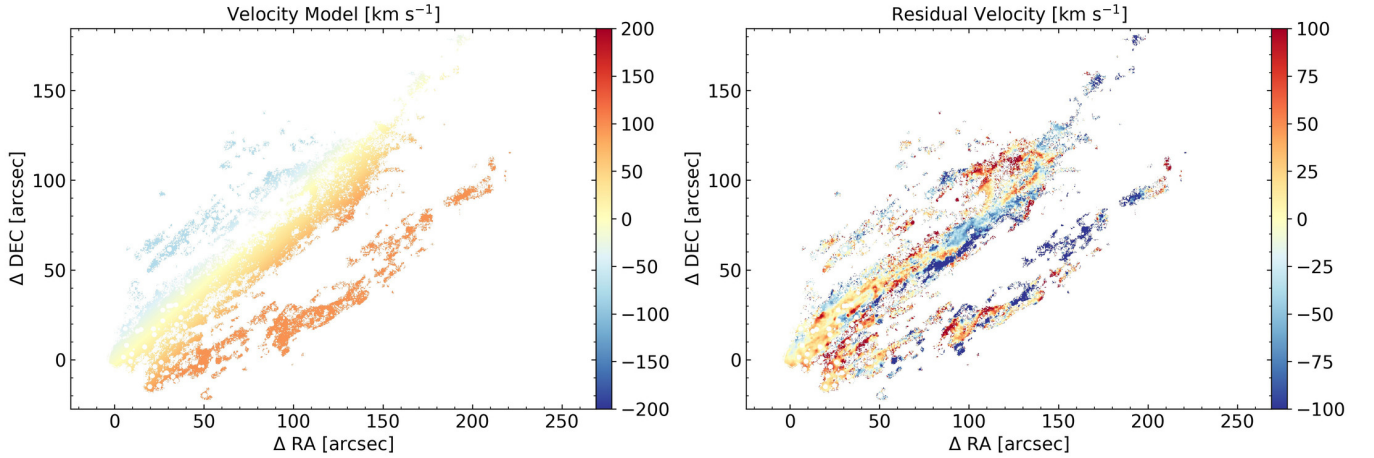


Figure 12. The velocity model of the ionized gas in ESO 137-001 and its stripped tails and the corresponding residual velocity field. The residual velocity field is obtained by subtracting the velocity model from the observed velocity field of the ionized gas.

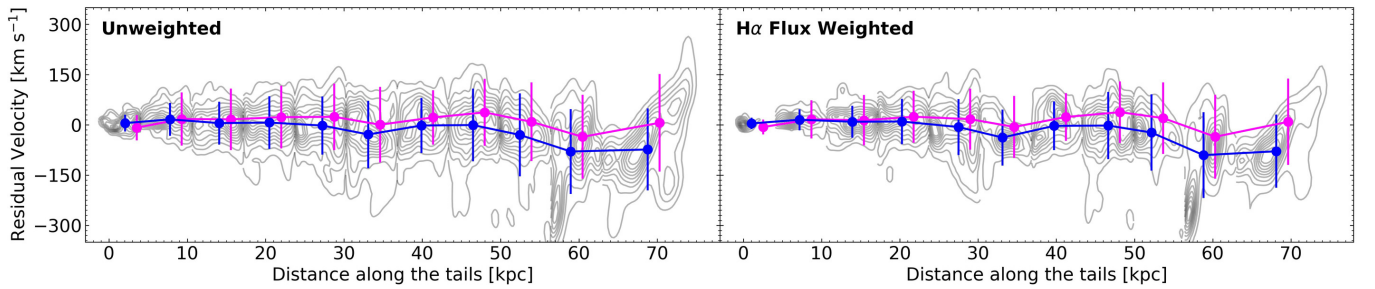


Figure 13. The kernel density estimation for the residual velocity (the right panel of Fig. 12) vs. the distance along the stripped tails. The contours are separated by 10%. The blue dots show the median values ± 1 sigma bars of the residual velocity in each region. The RMS of the median residual velocity is 35.5 km s^{-1} for unweighted and 39.1 km s^{-1} for weighted. The magenta dots present the median velocities ± 1 sigma bars as shown in Fig. 5, which are offset for comparison. The medians of the scatter ratios between the two curves (blue/magenta) are 0.87 for unweighted and 0.9 for weighted.

clearly deviates from the direction of the major axis of the stellar disc (PA: 42° vs. 9°). This result highlights the influence of RPS on the kinematic properties of stripped gas. Considering this point, for ESO 137-001, we suggest it is not sufficient to adopt the stellar velocity field itself as a reference to model the velocity field of ionized gas in the stripped tails. Although the velocity gradient in the stripped tails could be originated from the rotation motion of the galaxy disc,

the velocity vector in the direction where RPS acts must be taken into account.

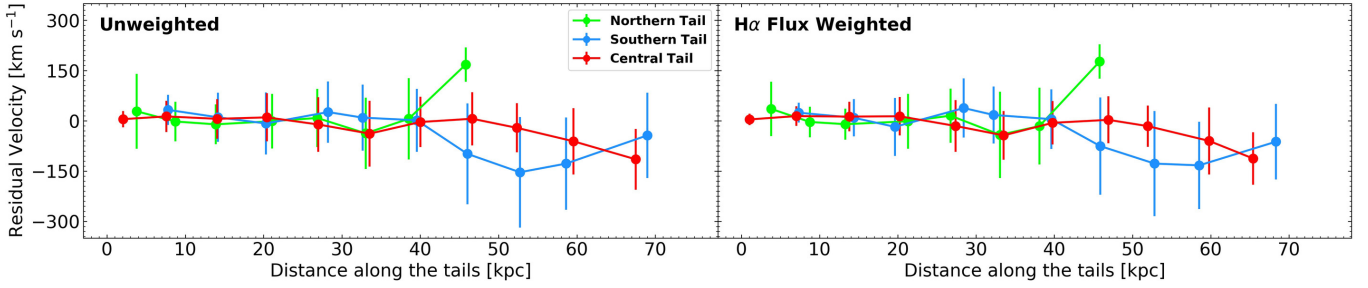


Figure 14. The median value of residual velocity in each tail vs. the distance along the stripped tails. The red, blue, and green dots show the median values ± 1 sigma bars of the residual velocity in each region from the central, the southern, and the northern tail, respectively. While the rotation pattern in the front part of the tails (within 40 kpc from the galaxy) is well corrected, it over-corrects the regions beyond.

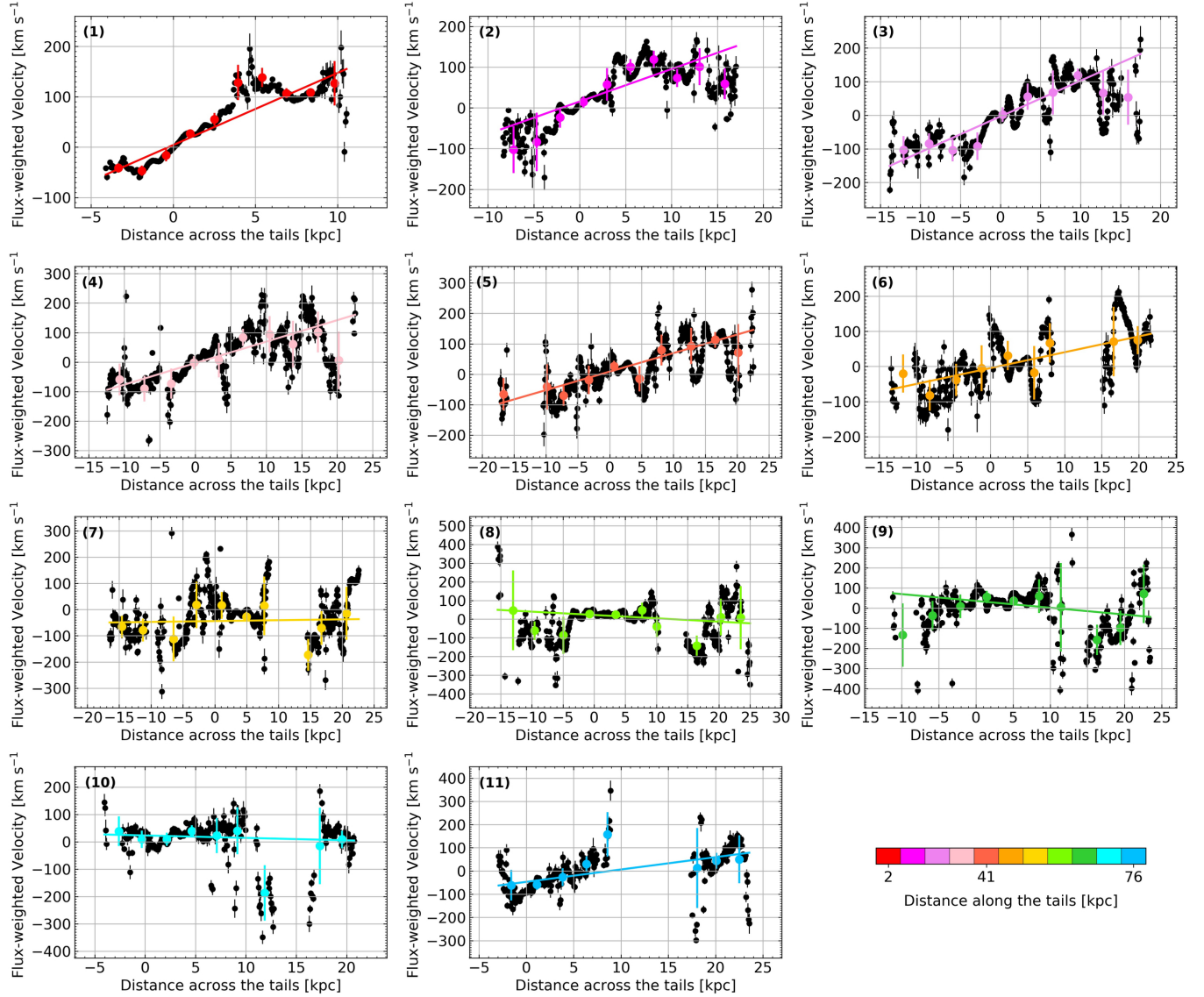


Figure 15. Fitting of the velocity gradient of the ionized gas in divided regions along the stripped tails of ESO 137-001. The positions of these regions are indicated by different colours. For each region, the black dots present the H α flux-weighted averages of the velocities from the spaxels in each column. The coloured dots show the error-weighted averages of the data in ten distance bins. The coloured line describes the best-fitting velocity gradient.

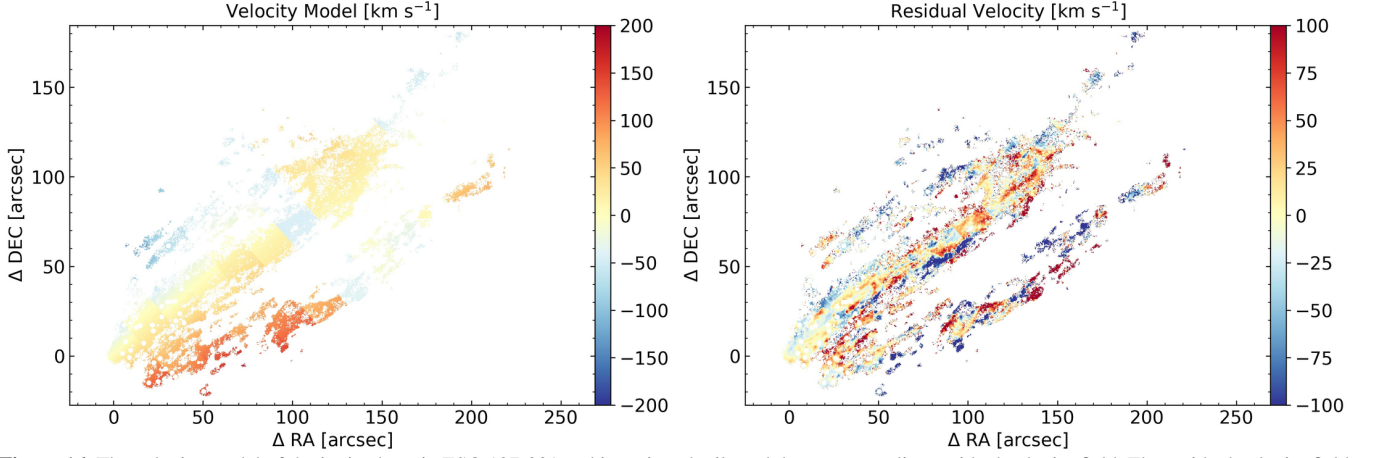


Figure 16. The velocity model of the ionized gas in ESO 137-001 and its stripped tails and the corresponding residual velocity field. The residual velocity field is obtained by subtracting the velocity model from the observed velocity field of the ionized gas.

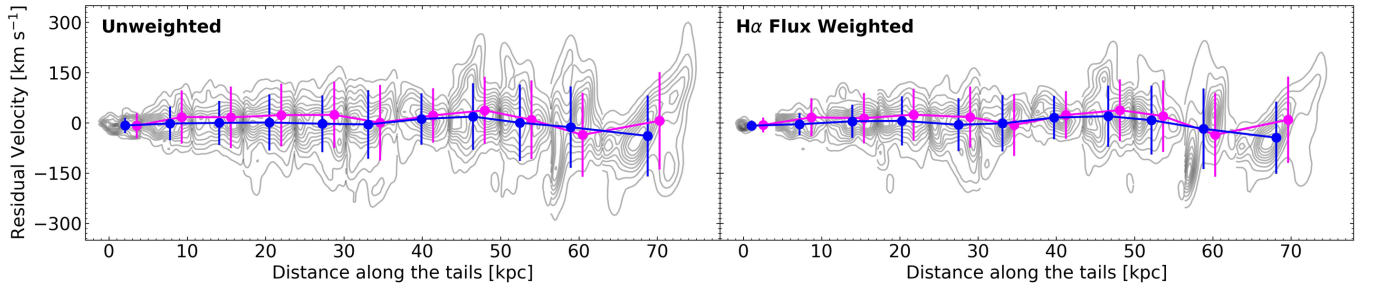


Figure 17. The kernel density estimation for the residual velocity (the right panel of Fig. 16) vs. the distance along the stripped tails. The contours are separated by 10%. The blue dots show the median values ± 1 sigma bars of the residual velocity in each region. The RMS of the median residual velocity are 14.4 km s^{-1} for unweighted and 16.9 km s^{-1} for weighted, which are significantly lower than those in the first method shown in Fig. 13 (as here blue points are close to zero than those in Fig. 13). The magenta dots present the median velocities ± 1 sigma bars as shown in Fig. 5, which are offset for comparison. The medians of the scatter ratios between the two curves (blue/magenta) are 0.89 for unweighted and 0.91 for weighted.

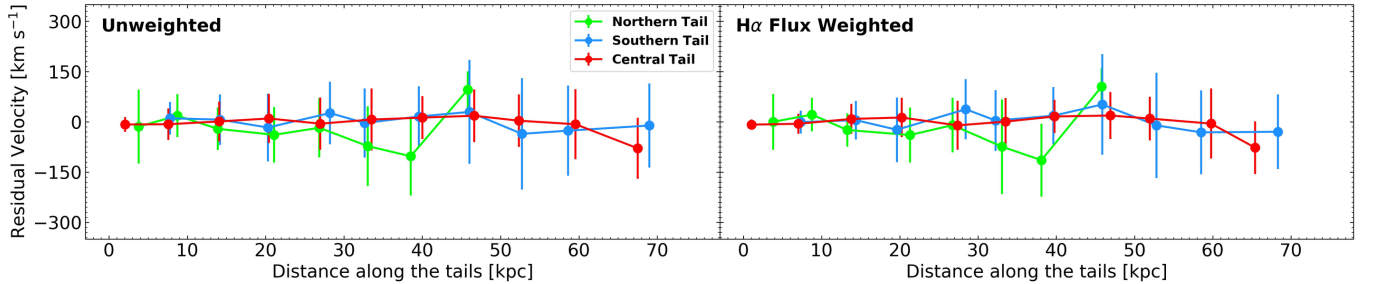


Figure 18. The median value of residual velocity in each tail vs. the distance along the stripped tails. The red, blue, and green dots show the median values ± 1 sigma bars of the residual velocity in each region from the central, the southern, and the northern tail, respectively. With the correction derived from Fig. 15, indeed the median velocities of different tails are now all consistent with zero.

3.3.2 Modelling based on the velocity gradients in different regions along the stripped tails

The above modeling can not trace the variation of velocity gradient along the stripped tails of ESO 137-001, which has been observed in Section 3.1. Thus, we attempted the second method to construct the velocity field model of the ionized gas. We first rotated 48° anticlockwise for the velocity field to ensure the global velocity gradient along the horizontal direction. Then we divided the velocity field into eleven regions along the stripped tails and measured the velocity gradients in these regions. We adopted the same width for the first ten regions, while the width of the last region was set to be larger to cover enough data points. As shown in Fig. 15, for each region,

we calculated the $H\alpha$ flux-weighted averages of the velocities from the spaxels in each column. The corresponding velocity gradient was derived by fitting these average velocities as a function of the distance across the stripped tails. We calculated the error-weighted averages of the data in ten distance bins and adopted a linear function to perform the fitting. The best-fitting velocity gradients of these regions are used to model the velocity field of the ionized gas.

The velocity field model of the ionized gas and its corresponding residual velocity field are shown in Fig. 16. We also performed similar kernel density estimations as those in Section 3.3.1 to examine the velocity field model. As presented in Fig. 17 and 18, the level of residual velocity is generally lower than that in the first method,

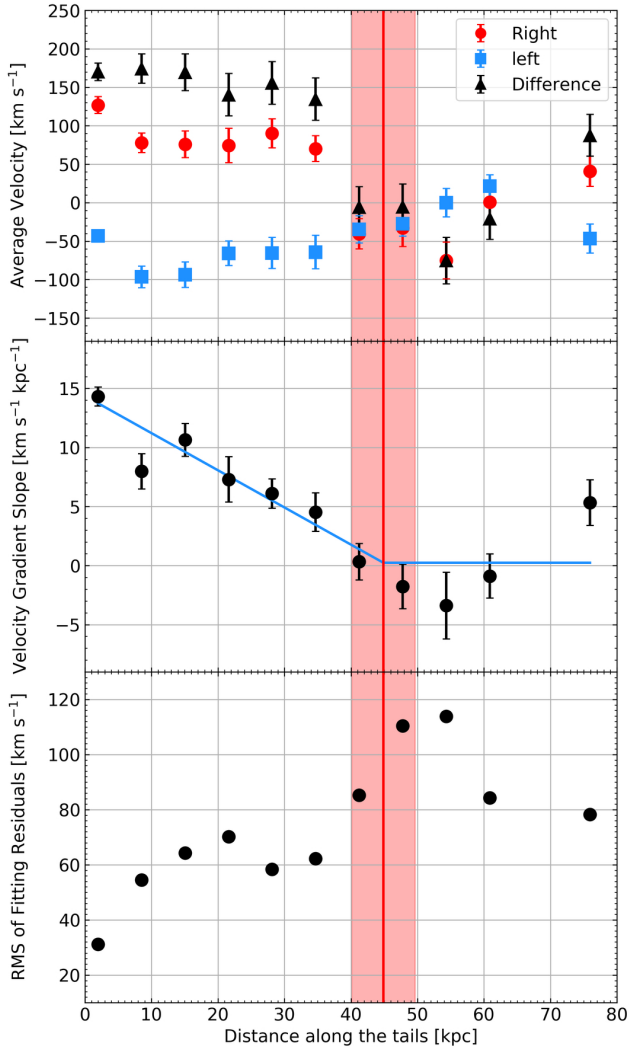


Figure 19. *Top:* The average velocities of the left and the right sides of the velocity curve in each region along the stripped tails in Fig. 15 and their differences. *Middle & Bottom:* The distributions of the slope of the velocity gradient and the RMS of the fitting residuals in Fig. 15 as a function of the distance along the stripped tails. The blue line shows the best-fitting distribution. The end point of the velocity gradient and its error are indicated by the red line and shaded red regions. We consider the red region (distance ~ 45 kpc) where the rotation pattern in the stripped warm, ionized gas has begun to disappear completely and the velocity field is fully at the mercy of turbulence.

especially in the rear half of the stripped tails, even the level of the remaining scatter is still comparable. In addition, the fluctuation of the median residual velocity along the stripped tails also becomes smaller. These results imply the second method can provide better modelling for the velocity field of the ionized gas. Note that the second method may potentially introduce more parameters in the velocity field model. A better velocity model could also be due to more regions being defined in the stripped tails (i.e. more parameters in the model). To avoid this effect, we constrained the number of regions in the above modelling to properly sample the variation of velocity gradient in the stripped tails. We also chose the appropriate region size to ensure enough data points are included in each region.

As shown in Fig. 15, the velocity gradient of the ionized gas changes along the stripped tails. In the first six regions, the velocity gradients are clearly shown and present a decreasing trend. While in

the last five regions, the velocity gradients become less significant. To further quantify this variation, we plotted the slope of the velocity gradient vs. the distance along the stripped tails in Fig. 19. The slope decreases as a function of the distance and becomes ~ 0 at the last five regions, suggesting the residual rotation imprint disappears beyond ~ 45 kpc from the galaxy. We adopted a piecewise function including a linear function and one plateau to fit the slope of the velocity gradient as a function of the distance along the stripped tails and obtained the end point of the velocity gradient at 44.9 ± 4.8 kpc. The corresponding RMS of residual velocity (observed velocity - velocity gradient) in the last five regions are generally larger than those in the first six regions, suggesting the small-scale velocity fluctuations increase in the rear half of the stripped tails. In the situation with strong velocity fluctuations, it could be difficult to identify the clear velocity gradient. We also calculate the average velocities of the left and the right sides of the velocity curve in each region along the stripped tails in Fig. 15 and their differences. Again, the difference nearly disappears beyond ~ 45 kpc. Thus, while the residual rotation inherited from the galaxy is observed to ~ 45 kpc from the galaxy, its imprint disappears beyond ~ 45 kpc. One may notice a potential velocity gradient in the last region of the stripped tails. This signature is only dominated by the small sections of data points at the ends of the central and southern tails. The trend of the velocity gradient increasing again is not clear.

4 DISCUSSION

4.1 The current state of the RPS tails

RPS has been considered as an outside-in process (see the review by Boselli et al. 2022). The less-denser ISM in the outer galaxy disc is more easily and early stripped by the ram pressure than the denser one in the inner galaxy disc. Thus, the medium stripped from different parts of the galaxy is at different evolutionary stages. The overall distribution and kinematics of the ionized gas in ESO 137-001 and its stripped tails support the above scenario, which has also been discussed by Fumagalli et al. (2014) and Jáchym et al. (2019). The width of the northern and southern tails is much larger with respect to the distribution of the ionized gas in the galaxy disc. In addition, the velocity of the ionized gas in these tails is generally more blueshifted or redshifted than that in the central tail. These observational signatures suggest an outer-disc origin for the northern and southern tails. The characteristic of the ionized gas in the galaxy disc indicates the gas content has been fully peeled off from the outer disc during the RPS process, while the ICM wind is still stripping the ionized gas from the inner galaxy disc to feed the central tail.

There are clear separations between the three stripped tails of ESO 137-001, which may imply the distribution of ISM in the galaxy is not continuous and one possibility involves the existence of an inner gas ring. For a barred galaxy, an inner ring structure is often observed at the corotation resonance and encircling the bar, with the active star formation and concentration of the ionized and cold gas (e.g. Combes & Gerin 1985; Buta & Combes 1996; Comerón et al. 2014). The morphology of ESO 137-001 is discussed in Waldron et al. (2023) with the *HST* data. There is no strong evidence for the existence of a bar but the inner morphology of the galaxy may be largely distorted by dust. The spilt of stripped tails may relate to the detailed ISM distributions in galaxies (Sun et al. 2010; Jáchym et al. 2014, 2019). In addition, other mechanisms may also contribute to the spilt of stripped tails, such as the effect of magnetic fields in producing the filamentary morphology of tails (e.g., Ruszkowski et al. 2014).

Based on the IFS observations of the front part of the primary tail,

Fumagalli et al. (2014) found the velocity dispersion of the ionized gas also shows an enhancement to ~ 20 kpc downstream and it can reach a peak value greater than 100 km s^{-1} beyond this distance. Our observations confirm this signature in the primary tail and present similar behaviours in the northern and southern tails, which show an increased velocity dispersion of the ionized gas from ~ 12 kpc to ~ 20 kpc downstream (see the velocity dispersion map in Fig. 3). The typical value of velocity dispersion increases from $\sim 35 \text{ km s}^{-1}$ to $\sim 80 \text{ km s}^{-1}$ and maintains the same level in the remaining part of the stripped tails. These results imply an enhancement of the degree of turbulence in the stripped tails, which could be due to the oscillations caused by the fallback gas flows in the galaxy wake. As shown in the hydrodynamic simulations of RPS tails, the interactions between the stripped tails and ambient ICM drive the gas moving into the shadow of the galaxy and induce the fallback gas flows (e.g., Roediger & Brügger 2007, 2008; Tonnesen & Bryan 2009; Roediger et al. 2015; Tonnesen 2019). The mixing between the fallback and forward gas flows produces oscillations in the striped tails and may increase the degree of turbulence. The analysis based on the velocity structure function will help to further understand the origin and evolution of turbulence in the stripped tails (e.g., Li et al. 2023).

4.2 The origin and implication of the velocity gradient decreasing in the stripped tails

The observations of the extraplanar gas in edge-on galaxies have shown its rotation velocity decreases along the vertical direction of the midplane of the galaxy (e.g., Heald et al. 2006; Oosterloo et al. 2007; Bizyaev et al. 2017; Levy et al. 2019; Marasco et al. 2019; Rautio et al. 2022). This velocity lag is considered as an important signature related to the origins of the extraplanar gas, which include the internal one - ejected through galaxy fountains (e.g., Shapiro & Field 1976; Bregman 1980), the external one - accretions from the IGM into the halo (e.g., Binney 2005; Kaufmann et al. 2006), and a combination of them (e.g., Fraternali & Binney 2008). For the extraplanar ionized gas, Levy et al. (2019) measured a median velocity lag of $21 \text{ km s}^{-1} \text{ kpc}^{-1}$ from a sample of 25 edge-on galaxies and also derived a median value of $25 \text{ km s}^{-1} \text{ kpc}^{-1}$ from the literature on the lag measurements. Based on the stellar rotation curve and the first velocity gradient in Fig. 15, we assumed an initial rotation velocity of $\sim 100 \text{ km s}^{-1}$ of the stripped gas. Considering this velocity becomes zero at ~ 45 kpc downstream (i.e., the place where the velocity gradient disappears), we thus derived a "velocity lag" as $\sim 2 \text{ km s}^{-1} \text{ kpc}^{-1}$, which suggests the velocity gradient decrease in the stripped tails is much slower than the velocity lag of the extraplanar gas. Since ESO 137-001 (thus the stripped gas) is moving much faster than the extraplanar gas, the relatively slow decrease of the velocity gradient in the stripped tails is not surprising. Another possible reason is that the stripped gas could be denser than the extraplanar gas. It is obvious that the place where the velocity gradient disappears is beyond the halo region of ESO 137-001. Thus, the effect of velocity lag in the galactic halo is not enough to account for the fading behaviour of the velocity gradient in the stripped tails. The velocity gradient itself introduces a velocity difference from that of the surrounding ICM, which can cause a local ram pressure to reduce the rotation motion of the stripped gas. This is probably another mechanism to explain the velocity gradient decrease in the stripped tails. Based on the high spectral resolution Fabry-Perot data, a vertical decrease in the rotation velocity of the stripped gas has also been discovered in the RPS galaxy NGC 4330, which is consistent with the hydrodynamic simulation of a face-on stripping process in this galaxy (Sardaneta et al. 2022).

From the velocity gradient decrease in the stripped tails of ESO 137-001, we can infer the kinematic evolution of the mixing between the stripped ISM and its ambient ICM. When the ISM is just stripped out from the galaxy, it can partially maintain the imprint of the galactic rotation, which is shown as the velocity gradient in the stripped tails. With the stripped gas moving away from the galaxy, its interactions with the ICM will gradually clean this imprint of the galactic rotation and make its kinematic behaviour similar to that of the ICM. As shown in the tails of ESO 137-001, the velocity gradient disappears beyond ~ 45 kpc downstream, where the stripped gas becomes co-moving with the ICM and kinematically mixed with it. For the stripped gas, we can estimate a mixing time-scale of ~ 90 Myr by assuming an average gas velocity of $\sim 500 \text{ km s}^{-1}$ along the tails (e.g., Tonnesen & Bryan 2010).

Gronke & Oh (2018) gave a characteristic radius for the embedded cold clouds to survive via growth from cooling, $r_{\text{crit}} \approx 20 \text{ pc } T_{\text{cl},4}^{5/2} \mathcal{M} P_{\text{ICM},4}^{-1} \Lambda_{\text{mix},-21.4}^{-1} (\chi/10^4)$, where $T_{\text{cl},4}$ is the cloud temperature in the unit of 10^4 K , \mathcal{M} is the Mach number of the cloud, $P_{\text{ICM},4}$ is the ICM pressure in the unit of 10^4 K cm^{-3} , $\Lambda_{\text{mix},-21.4}$ is the cooling function in the unit of $10^{-21.4} \text{ erg cm}^3 \text{ sec}^{-1}$, and χ is the density contrast between the cloud and the ICM. For the stripped clouds behind ESO 137-001, we assume $T_{\text{cl},4}=1$, $n_{\text{e,ICM}} = 10^{-3} \text{ cm}^{-3}$, $T_{\text{ICM}} = 7 \times 10^7 \text{ K}$, $\Lambda_{\text{mix}} = 10^{-21.8} \text{ erg cm}^3 \text{ sec}^{-1}$ which is roughly the cooling function at $T_{\text{mix}} \approx \sqrt{T_{\text{ICM}} T_{\text{cl}}} = 8 \times 10^5 \text{ K}$, and $\chi = T_{\text{ICM}}/T_{\text{cl}} = 7 \times 10^3$. Thus, $r_{\text{crit}} \approx 2.6 \mathcal{M} \text{ pc}$. We note that this scale is very similar to the characteristic scale of the H α emitting gas estimated by Sun et al. (2022). Stripped clouds are subject to local ram pressure. The drag time $t_{\text{drag}} \sim \chi r / v_{\text{cl}}$, while v_{cl} is the velocity of the cloud relative to the local surrounding medium and r is the radius the cloud. Assuming the relative velocity between the stripped cloud and the galaxy is v_{rel} , the *MUSE* results suggest that $t_{\text{drag}} v_{\text{rel}} \approx 45 \text{ kpc}$. We can write $t_{\text{drag}} v_{\text{rel}} = 42 \text{ kpc } (\chi / 7 \times 10^3) (r / 2 \text{ pc}) (\frac{v_{\text{rel}}/v_{\text{cl}}}{3})$, while the last ratio can be understood if $v_{\text{rel}} \sim 500 \text{ km s}^{-1}$ as discussed above and $v_{\text{cl}} \sim 150 \text{ km s}^{-1}$ from the galactic rotation at > 8 kpc from the nucleus. Note that this estimate considered only ram pressure whereas mass transfer via cooling leads generally to a faster entrainment. More detailed modeling and comparison with simulations are required in the future to better understand the change of the velocity gradient observed in stripped tails.

4.3 The connection of warm, ionized gas with gas at other phases

Based on the *ALMA* observations of CO(2-1) emission, the cold molecular gas has been detected to ~ 60 kpc along the stripped tails of ESO 137-001 (Jáchym et al. 2019). To explore the kinematics connection between the warm ionized gas and cold molecular gas in the stripped tails, we selected 68 regions detected in both CO from *ALMA* and optical emission lines from *MUSE*, and compared the velocity and velocity dispersion between these two gas phases. Note our comparison involves the kinematic quantities along the LOS. Since the warm, ionized gas has a much larger covering fraction than the cold molecular gas, the region selection is limited by the *ALMA* data at regions with significant CO detection and a single velocity. The velocity and the FWHM (or 2.355σ for a Gaussian profile) of the gas content are measured from the integrated spectra of individual regions. As shown in Fig. 20, the velocities of the two gas phases generally agree within 30 km s^{-1} , with the RMS of the velocity difference of $\sim 16 \text{ km s}^{-1}$. In addition, this velocity difference is not related to the specific location of the gas content. These results sug-

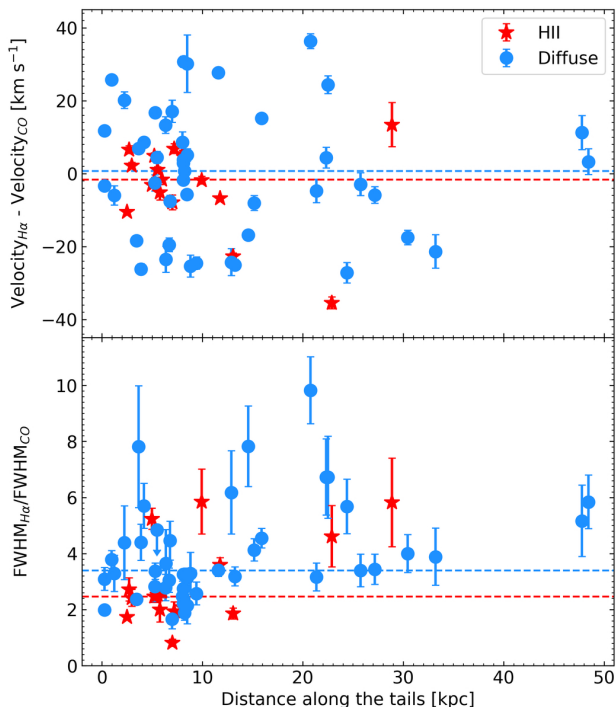


Figure 20. For 68 regions in ESO 137-001’s tail detected in both CO from *ALMA* and optical emission lines from *MUSE*, we compare their velocities (top panel) and velocity dispersion (bottom panel). The velocity precision of *MUSE* is 2.5–4.0 km s^{−1} (Weilbacher et al. 2020), while *ALMA* has a much higher precision (Jáchym et al. 2019). The generally small velocity difference between the two gas phases suggests they are mostly co-moving through the tails. The larger velocity dispersion for the warm, ionized gas than that of the cold, molecular gas can be caused by projection.

gest that the ionized gas and molecular gas are not only co-spatial but also co-moving through the tails, which provides further kinematic evidence of the mixing between different gas phases in the stripping process. As discussed in Jáchym et al. (2019), a part of the molecular gas is formed in situ, thus its velocity is naturally coincident with other gas phases. For the part of molecular gas stripped from the galaxy disc, the velocity coincidence with the ionized gas may also imply that two gas phases are stripped around the same time. The FWHM of ionized gas is typically higher than that of molecular gas, with a median ratio of ~ 3.3 . Such kind of difference in velocity dispersion has also been observed in the gas filaments of the cool core clusters (e.g. Tremblay et al. 2018; Olivares et al. 2019). The possible reason is due to the projection effect of different spatial distributions between the different gas phases (e.g., each LOS catches many tiny ionized gas clouds but only one big molecular cloud). Gaspari et al. (2018) shows that warm ionized gas is likely to be more turbulent than cold molecular gas in the filaments. Li et al. (2023) compared the velocity structure functions of the ionized gas and molecular gas in the stripped tails of ESO 137-001 and reached a similar conclusion.

By separating the gas content associated with the H II regions and diffuse regions, we also examine if the above comparisons are different between these two kinds of regions. The velocity differences between the ionized gas and molecular gas have similar median values (-1.6 km s^{−1} in H II regions vs. 0.7 km s^{−1} in diffuse regions), but different scatter (RMS: 11.8 km s^{−1} in H II regions vs. 17.4 km s^{−1} in diffuse regions). The general small velocity difference suggests the co-moving of two gas phases in these regions. For the diffuse regions, the velocity dispersion ratio between the ionized gas

and molecular gas is larger than that in the H II regions (median values: 3.4 vs. 2.5), which may be related to projection and the more turbulent environment of the diffuse gas.

5 CONCLUSIONS

By combining our new *MUSE* observations and the archived data, we construct a large mosaic to cover ESO 137-001 and its RPS tails. We studied the distribution and kinematic properties of the ionized gas and stars, and linked them with the RPS process in ESO 137-001 as well as the substructures of the stripped tails. The main results are summarised as follows.

The stripped ionized gas of ESO 137-001 splits into three tails. While the central and southern tails can extend to at least ~ 87 kpc and ~ 75 from the galaxy centre and present good continuity, the northern tail is more clumpy and contains several filament substructures, which cover a region of ~ 5 kpc \times 40 kpc. Based on the kernel density estimation, we studied the distributions of the gas velocity and velocity dispersion along the stripped tails. The median velocity of the ionized gas does not significantly change along the stripped tails, which confirms the galaxy is mainly moving on the sky plane. While the median velocity dispersion of the ionized gas increases from ~ 35 km s^{−1} in the galaxy disc to ~ 80 km s^{−1} at ~ 20 kpc downstream and maintains a similar level in the rest of the stripped tails, suggesting an enhancement of the degree of the turbulence within this distance. The spreads of the velocity and velocity dispersion in the stripped tails are generally larger than those in the galaxy disc, which is consistent with the predictions in the simulations of RPS tails.

In the galaxy disc of ESO 137-001, significant differences are shown between the distributions and velocity fields of the ionized gas and stars, indicating the intense perturbations produced by RPS and this process is already well advanced. While the stars are well located in a rotating disc, most ionized gas in the outer galaxy disc has been stripped. Ram pressure shapes the remnant ionized gas into a narrow cone, which connects the inner galaxy disc with the central tail. The velocity differences between the ionized gas and stars present a clear enhancement from ~ 0 km s^{−1} in the inner galaxy disc to ~ 40 km s^{−1} in the outer galaxy disc, which provides a potential hint of gas deceleration due to RPS.

The velocity field of the ionized gas presents a clear velocity gradient roughly perpendicular to the stripping direction, which ranges from an average value of ~ -80 km s^{−1} in the northern tail to ~ 120 km s^{−1} in the southern tail. This velocity gradient linearly decreases along the stripped tails and disappears at 44.9 ± 4.8 kpc downstream. The velocity range of this gradient is generally consistent with that of the stellar rotation curve, indicating it originates from the rotation motion of the galaxy disc. We constructed the velocity model for the above residual galactic rotation based on: (1) the global velocity gradient in the front part of the stripped tails; (2) the velocity gradients in different regions along the stripped tails. The second model provides less residuals after subtracting the observed velocity field, suggesting it is better than the first one.

The observed results of ESO 137-001 and its stripped tails support the outside-in scenario of RPS. The ionized gas in the outer disc has been fully stripped to form the northern and southern tails, while the central tail is built with the ionized gas from the inner galaxy disc, which is still feeding the stripping process. By comparing with the simulated RPS tails, we interpreted that the enhanced velocity dispersion in the stripped tails of ESO 137-001 could be a result of the oscillations induced by the fallback gas flows in the galaxy wake.

We discuss the possible origins of the velocity gradient decreasing in the stripped tails, which include the rotation velocity lag within the galaxy halo and the effect of local ram pressure caused by the interaction with ambient ICM. The decreasing velocity gradient in the stripped tails also implies the kinematic evolution of the mixing between the stripped ISM and its ambient ICM. The comparison of kinematic properties between the warm ionized gas and cold molecular gas shows that they are co-moving through the stripped tails, which provides further kinematic evidence of the mixing between different gas phases in the stripping process.

Our research demonstrates the great potential of wide-field optical integral-field spectroscopy in probing the detailed distribution and kinematic properties of ionized gas (i.e., warm phase) in RPS. With the ongoing development of spatially resolved spectroscopy in X-ray, IR, and radio (e.g., *Athena*, *JWST*, *SKA*, and *ALMA*), future multi-wavelength campaigns will provide a comprehensive picture of the kinematic properties of the multi-phase stripped medium, which will further shed light on the role of gas kinematics in their mixing and evolution and provides important information for future simulations of RPS.

ACKNOWLEDGEMENTS

We thank the referee for detailed and useful comments. Support for this work was provided by the NSF grant 1714764 and the NASA grants 80NSSC21K0704 and 80NSSC19K1257. P.J. acknowledges support from the project RVO:67985815, and the project LM2023059 of the Ministry of Education, Youth and Sports of the Czech Republic. M.F. and M.F. acknowledge support from the European Research Council (ERC) under the European Union's Horizon 2020 research and innovation programme (grant agreement No 757535). Y.L. acknowledges financial support from NSF grants AST-2107735 and AST-2219686, and NASA grant 80NSSC22K0668. This research is based on observations collected at the European Southern Observatory under ESO programme 095.A-0512(A), 0104.A-0226(A), 60.A-9349(A) and 60.A-9100(G).

DATA AVAILABILITY

The *MUSE* raw data are available to download at the ESO Science Archive Facility⁷. The reduced data underlying this paper will be shared on reasonable requests to the corresponding authors.

REFERENCES

Bacon R., et al., 2010, in McLean I. S., Ramsay S. K., Takami H., eds, Society of Photo-Optical Instrumentation Engineers (SPIE) Conference Series Vol. 7735, Ground-based and Airborne Instrumentation for Astronomy III. p. 773508, doi:10.1117/12.856027

Bacon R., Piqueras L., Conseil S., Richard J., Shepherd M., 2016, MPDAF: MUSE Python Data Analysis Framework, Astrophysics Source Code Library, record ascl:1611.003 (ascl:1611.003)

Begeman K. G., 1987, PhD thesis, University of Groningen, Kapteyn Astronomical Institute

Bekki K., Couch W. J., 2003, *ApJL*, 596, L13

Bellhouse C., et al., 2017, *ApJ*, 844, 49

Bellhouse C., et al., 2021, *MNRAS*, 500, 1285

Binney J., 2005, in Braun R., ed., Astronomical Society of the Pacific Conference Series Vol. 331, Extra-Planar Gas. p. 131 (arXiv:astro-ph/0409639)

Bizyaev D., et al., 2017, *ApJ*, 839, 87

Boselli A., Gavazzi G., 2006, *PASP*, 118, 517

Boselli A., Boissier S., Cortese L., Gavazzi G., 2008, *ApJ*, 674, 742

Boselli A., et al., 2018, *A&A*, 615, A114

Boselli A., et al., 2021, *A&A*, 646, A139

Boselli A., Fossati M., Sun M., 2022, *A&ARv*, 30, 3

Bosma A., 1978, PhD thesis, University of Groningen, Netherlands

Bregman J. N., 1980, *ApJ*, 236, 577

Buta R., Combes F., 1996, *Fundamentals Cosmic Phys.*, 17, 95

Cappellari M., 2017, *MNRAS*, 466, 798

Cappellari M., Copin Y., 2003, *MNRAS*, 342, 345

Cappellari M., Emsellem E., 2004, *PASP*, 116, 138

Chabrier G., 2003, *PASP*, 115, 763

Combes F., Gerin M., 1985, *A&A*, 150, 327

Comerón S., et al., 2014, *A&A*, 562, A121

Consolandi G., Gavazzi G., Fossati M., Fumagalli M., Boselli A., Yagi M., Yoshida M., 2017, *A&A*, 606, A83

Domainko W., et al., 2006, *A&A*, 452, 795

Dressler A., 1980, *ApJ*, 236, 351

ESO CPL Development Team 2015, EsoRex: ESO Recipe Execution Tool, Astrophysics Source Code Library, record ascl:1504.003 (ascl:1504.003)

Fitzpatrick E. L., 1999, *PASP*, 111, 63

Fossati M., Fumagalli M., Boselli A., Gavazzi G., Sun M., Wilman D. J., 2016, *MNRAS*, 455, 2028

Fossati M., et al., 2018, *A&A*, 614, A57

Fossati M., Fumagalli M., Gavazzi G., Consolandi G., Boselli A., Yagi M., Sun M., Wilman D. J., 2019, *MNRAS*, 484, 2212

Fraternali F., Binney J. J., 2008, *MNRAS*, 386, 935

Fumagalli M., Fossati M., Hau G. K. T., Gavazzi G., Bower R., Sun M., Boselli A., 2014, *MNRAS*, 445, 4335

Gaspari M., et al., 2018, *ApJ*, 854, 167

Gavazzi G., Contursi A., Carrasco L., Boselli A., Kennicutt R., Scodreggio M., Jaffe W., 1995, *A&A*, 304, 325

Ge C., et al., 2021, *MNRAS*, 505, 4702

Gronke M., Oh S. P., 2018, *MNRAS*, 480, L111

Gullieuszik M., et al., 2017, *ApJ*, 846, 27

Gunn J. E., Gott J. Richard I., 1972, *ApJ*, 176, 1

Haan S., Braun R., 2014, *MNRAS*, 440, L21

Heald G. H., Rand R. J., Benjamin R. A., Bershadsky M. A., 2006, *ApJ*, 647, 1018

Jáchym P., Combes F., Cortese L., Sun M., Kenney J. D. P., 2014, *ApJ*, 792, 11

Jáchym P., et al., 2019, *ApJ*, 883, 145

Kapferer W., et al., 2007, *A&A*, 466, 813

Kaufmann T., Mayer L., Wadsley J., Stadel J., Moore B., 2006, *MNRAS*, 370, 1612

Krajnović D., Cappellari M., de Zeeuw P. T., Copin Y., 2006, *MNRAS*, 366, 787

Kronberger T., Kapferer W., Unterguggenberger S., Schindler S., Ziegler B. L., 2008, *A&A*, 483, 783

Lee J., Kimm T., Katz H., Rosdahl J., Devriendt J., Slyz A., 2020, *ApJ*, 905, 31

Levy R. C., et al., 2019, *ApJ*, 882, 84

Lewis I., et al., 2002, *MNRAS*, 334, 673

Li Y., Luo R., Fossati M., Sun M., Jáchym P., 2023, accepted for publication in *MNRAS*, <https://arxiv.org/abs/2303.15500>

Liu Q., et al., 2021, *ApJ*, 908, 228

Marasco A., et al., 2019, *A&A*, 631, A50

Merluzzi P., et al., 2013, *MNRAS*, 429, 1747

Olivares V., et al., 2019, *A&A*, 631, A22

Oosterloo T., Fraternali F., Sancisi R., 2007, *AJ*, 134, 1019

Pietrinferni A., Cassisi S., Salaris M., Castelli F., 2004, *ApJ*, 612, 168

Poggianti B. M., et al., 2017, *ApJ*, 844, 48

Quilis V., Moore B., Bower R., 2000, *Science*, 288, 1617

⁷ <http://archive.eso.org/cms.html>

- Rautio R. P. V., Watkins A. E., Comerón S., Salo H., Díaz-García S., Janz J., 2022, *A&A*, **659**, A153
- Roediger E., Brüggen M., 2007, *MNRAS*, **380**, 1399
- Roediger E., Brüggen M., 2008, *MNRAS*, **388**, 465
- Roediger E., et al., 2015, *ApJ*, **806**, 103
- Rogstad D. H., Lockhart I. A., Wright M. C. H., 1974, *ApJ*, **193**, 309
- Ruszkowski M., Brüggen M., Lee D., Shin M. S., 2014, *ApJ*, **784**, 75
- Sarazin C. L., 1986, *Reviews of Modern Physics*, **58**, 1
- Sardaneta M. M., et al., 2022, *A&A*, **659**, A45
- Schindler S., et al., 2005, *A&A*, **435**, L25
- Schlafly E. F., Finkbeiner D. P., 2011, *ApJ*, **737**, 103
- Schlegel D. J., Finkbeiner D. P., Davis M., 1998, *ApJ*, **500**, 525
- Schoenmakers R. H. M., Franx M., de Zeeuw P. T., 1997, *MNRAS*, **292**, 349
- Shapiro P. R., Field G. B., 1976, *ApJ*, **205**, 762
- Sivanandam S., Rieke M. J., Rieke G. H., 2010, *ApJ*, **717**, 147
- Soto K. T., Lilly S. J., Bacon R., Richard J., Conseil S., 2016, *MNRAS*, **458**, 3210
- Sun M., Jones C., Forman W., Nulsen P. E. J., Donahue M., Voit G. M., 2006, *ApJL*, **637**, L81
- Sun M., Donahue M., Voit G. M., 2007, *ApJ*, **671**, 190
- Sun M., Donahue M., Roediger E., Nulsen P. E. J., Voit G. M., Sarazin C., Forman W., Jones C., 2010, *ApJ*, **708**, 946
- Sun M., et al., 2022, *Nature Astronomy*, **6**, 270
- Tonnesen S., 2019, *ApJ*, **874**, 161
- Tonnesen S., Bryan G. L., 2009, *ApJ*, **694**, 789
- Tonnesen S., Bryan G. L., 2010, *ApJ*, **709**, 1203
- Tremblay G. R., et al., 2018, *ApJ*, **865**, 13
- Vazdekis A., Koleva M., Ricciardelli E., Röck B., Falcón-Barroso J., 2016, *MNRAS*, **463**, 3409
- Vazza F., Eckert D., Simionescu A., Brüggen M., Ettori S., 2013, *MNRAS*, **429**, 799
- Waldron W., Sun M., Luo R., et al., 2023, accepted for publication in *MNRAS*, <https://arxiv.org/abs/2302.07270>
- Weilbacher P. M., Streicher O., Urrutia T., Jarno A., Pécontal-Rousset A., Bacon R., Böhm P., 2012, in Radziwill N. M., Chiozzi G., eds, *Society of Photo-Optical Instrumentation Engineers (SPIE) Conference Series Vol. 8451, Software and Cyberinfrastructure for Astronomy II*. p. 84510B, doi:10.1117/12.925114
- Weilbacher P. M., et al., 2020, *A&A*, **641**, A28
- Wong T., Blitz L., Bosma A., 2004, *ApJ*, **605**, 183
- Woudt P. A., Kraan-Korteweg R. C., Cayatte V., Balkowski C., Felenbok P., 2004, *A&A*, **415**, 9
- Woudt P. A., Kraan-Korteweg R. C., Lucey J., Fairall A. P., Moore S. A. W., 2008, *MNRAS*, **383**, 445

This paper has been typeset from a $\text{\TeX}/\text{\LaTeX}$ file prepared by the author.